Rep. Prog. Phys. **62** (1999) 237–276. Printed in the UK PII: S0034-4885(99)55214-7

Transport properties of dilute alloys

Ingrid Mertig
Institut für Theoretische Physik, TU Dresden, D-01062 Dresden, Germany

Received 15 September 1998

Abstract

The review introduces the reader to a theoretical method describing the transport properties of dilute alloys on an *ab initio* basis. The calculations start from density or spin density functional theory using a Green function formalism to investigate the underlying electronic structure of the ideal and perturbed system on equal footing. The residual resistivity is calculated solving the quasiclassical Boltzmann equation. The theory is outlined and various methods and approximations developed to solve the transport equation are reviewed and compared with respect to accuracy and validity. It will be demonstrated that the theory is able to quantitatively account. The success and limitations of these calculations are discussed for a large variety of systems, non-magnetic and ferromagnetic, in comparison with experimental results. It will be shown that these calculations confirm empirical rules and concepts, elucidate the microscopic processes behind the trends and can be used to make a theoretical material design.

0034-4885/99/020237+40$59.50

Contents

1. Introduction

Resistivity is one of the most important quantities, a fingerprint, to characterize a metallic system. It is relatively easy to measure and contains a wealth of information about electrons and their interactions with other quasiparticles in the system. At zero temperature many of these interactions, for example lattice vibrations and magnons, are frozen out. The so-called residual resistivity is obtained. The residual resistivity is caused by impurities, other lattice imperfections or substitutional disorder. The residual resistivity of an ideal metallic system would be zero. But that never happens in reality. Because of the significance of the residual resistivity a huge variety of highly precise experimental data exists [1].

The theoretical description of transport properties was less developed since it is a task of considerable complexity. Due to the influence of the external electric field the systems are no longer in thermodynamic equilibrium. Principles of irreversible thermodynamics have to be included [2–4]. Consequently, simple phenomenological models have been used to explain the experimental data.

Within Drude's classical theory of transport a diffusive motion of electrons under the influence of the external field and the scattering processes is assumed. The resistivity is described by two parameters only. The relaxation time τ, a parameter for the scattering, and the velocity of the electrons v_F. Usually both parameters are combined to the mean free path $\Lambda = \tau v_F$, the path of the electron between two scattering events. Obviously, this model is too easy to account for the variety of experimental results since it neglects details of the electronic structure of the system all together.

More powerful concepts are the so-called quasiclassical or the fully quantum mechanical description. In the first case the electrons are considered quantum mechanically and the response to the external field is included in a classical manner. A kinetic equation like the Boltzmann equation has to be solved. The fully quantum mechanical description, however, is based on Kubo's formula [5]. In both cases a linear response to the external field is assumed. The first approach is limited to cases where the mean free path of the electrons is large in comparison with the lattice spacing and therefore to cases of weak disorder, for example dilute alloys. The latter case is free of such limitations and can also be applied to strongly disordered systems. It was shown [6,7] that both methods are equivalent if the mean free path is large in comparison to the lattice spacing and small with respect to the sample dimension.

These methods combined with the advantages of density functional theory are powerful tools and allow us to describe transport properties on an *ab initio* basis, that is, without any free parameter. Applications to various dilute and concentrated alloy systems demonstrate that the theories allow for a parameter-free treatment of transport and yield numerical results which are in good agreement with experimental data [8–13]. The aim of this review is to make the reader familiar with the formalism and the high quality of the *ab initio* calculations of transport properties for dilute alloys based on solution of the Boltzmann equation.

The electronic structure of dilute alloys necessary to solve the Boltzmann equation can be described very efficiently by density functional theory formulated within a Green function method [14–19]. A Green function method is especially suited since the electronic structure of the ideal, translationally invariant system and of the perturbed system, the system with an impurity, that is, with broken translational symmetry may be calculated on equal footing. Both components form the input to compute the impurity scattering matrix elements and to solve the Boltzmann equation [8,12,20,21]. The connection of transport properties with anisotropic electronic structure and the anisotropy of impurity scattering is illustrated in great detail. It will be shown that these calculations elucidate the microscopic processes behind transport in a fantastic manner, confirm empirical rules and can be used to make a theoretical material design.

The review is organized as follows. A short summary of the underlying concept of density functional theory and the Green function method is given in section 2. Section 3 is an introduction to the Boltzmann equation and a discussion of various methods and approximations developed to solve the transport equation. A collection of results for non-magnetic and ferromagnetic systems is presented in section 4.

2. Theory and method underlying the calculation

In order to develop a parameter-free method which enables us to calculate the transport properties of metallic systems several aspects need to be considered. One of which is the solution of the electronic structure problem for the translationally invariant system. The fundamental concept behind all electronic structure methods is density functional theory. The second one is the consideration of imperfect systems. We concentrate, in particular, on the description of point defects in metals. Point defects break the translational symmetry of the ideal host and the band structure methods can no longer be applied. It has been shown that the multiple scattering theory is a powerful method to describe the scattering of Bloch waves in perturbed systems.

This chapter is dedicated to elucidate these underlying concepts.

2.1. Density functional theory

The problem one needs to solve is the many-body problem of a system formed by the interacting electrons and nuclei. With the Born–Oppenheimer approximation [22] the problem can be reduced to a system of N interacting electrons moving in the electrostatic potential V_{ext} caused by the nuclei

$$H = \sum_{i=1}^{N} \left(-\frac{\hbar^2}{2m} \right) \frac{\partial^2}{\partial \boldsymbol{r}_i^2} + \sum_{i=1}^{N} V_{\text{ext}}(\boldsymbol{r}_i) + \frac{1}{2} \sum_{i \neq j}^{N} \frac{\epsilon^2}{|\boldsymbol{r}_i - \boldsymbol{r}_j|} \tag{1}$$

where $\epsilon^2 = e^2/4\pi\epsilon_0$. ϵ_0 is the dielectric constant. $\boldsymbol{r}_i$ is the position of electron i while all other constants have their traditional meaning.

Density functional theory (Hohenberg and Kohn [23], Kohn and Sham [24], Sham and Kohn [25]) constitutes the main underlying basis for the solution of this problem.

The theory is founded on the Hohenberg–Kohn theorem [23] which states that the ground state energy of a many-body system is a unique functional of the one-particle charge density $n(\boldsymbol{r})$. The ground state energy can be derived from a variational principle

$$E[V_{\text{ext}}] = \min_{n(\boldsymbol{r})} \left(\int \mathrm{d}^3 r \; V_{\text{ext}} n(\boldsymbol{r}) + F[n] \right) \tag{2}$$

where $F[n]$ is a unique functional of the charge density $n(\boldsymbol{r})$ independent of the external potential V_{ext} which can be expressed as [24]

$$F[n] = T[n] + U[n] + E_{xc}[n]. \tag{3}$$

Here, $T[n]$ is the functional of the kinetic energy for a set of N non-interacting electrons of density $n(\boldsymbol{r})$. $U[n]$ is the classical Hartree energy

$$U[n] = \frac{1}{2} \int \mathrm{d}^3 r \, n(\boldsymbol{r}) \int \mathrm{d}^3 r' \, n(\boldsymbol{r}') \frac{\epsilon^2}{|\boldsymbol{r} - \boldsymbol{r}'|} \tag{4}$$

and $E_{xc}[n]$ the exchange-correlation energy which includes all many-body interactions, exchange and correlation, in an effective way. Variation of the ground state energy, under the assumption of a charge density being a sum over all occupied single-particle states [24]

$$n(\boldsymbol{r}) = 2\sum_{k}^{\text{occ}} |\varphi_k(\boldsymbol{r})|^2 \tag{5}$$

with the single-particle wavefunctions $\varphi_k(\boldsymbol{r})$ for an arbitrary set of quantum numbers k, leads to the well known Kohn–Sham equations

$$\left[-\frac{\hbar^2}{2m}\frac{\partial^2}{\partial \boldsymbol{r}^2} + V(\boldsymbol{r})\right]\varphi_k(\boldsymbol{r}) = E_k\varphi_k(\boldsymbol{r}). \tag{6}$$

These equations describe the motion of independent particles in an effective potential

$$V(\boldsymbol{r}) = V_{\text{ext}}(\boldsymbol{r}) + \int \mathrm{d}^3r'\, n(\boldsymbol{r}')\frac{\epsilon^2}{|\boldsymbol{r}-\boldsymbol{r}'|} + V_{xc}(\boldsymbol{r}) \tag{7}$$

with

$$V_{xc}(\boldsymbol{r}) = \frac{\delta E_{xc}[n(\boldsymbol{r})]}{\delta n(\boldsymbol{r})}, \tag{8}$$

which is a functional of the single-particle wavefunctions through $n(\boldsymbol{r})$. Solving these equations the charge density $n(\boldsymbol{r})$ and the ground state energy $E[n(\boldsymbol{r})]$ can be obtained iteratively.

Physically, the Lagrange parameters E_k, which result from the constraint that the particle number be conserved, are meaningless here serving simply as a device to solve the underlying self-consistent problem. Under some special circumstances though [24,26,27], the eigenvalues and eigenfunctions can be used to approximate the quasi-particle band structures of real materials.

This set of single-particle Kohn–Sham equations would, in principle, provide the exact solution to the many-body problem if the functional form of the exchange-correlation potential were known exactly. Since it is not, approximations such as the local density approximation have been introduced. For slowly varying charge densities, the ground state energy $E_{xc}[n]$ can be approximated by

$$E_{xc}[n] \approx \int \mathrm{d}^3r\, n(\boldsymbol{r})\epsilon_{xc}^{\text{hom}}(n(\boldsymbol{r})), \tag{9}$$

where $\epsilon_{xc}^{\text{hom}}$ is the exchange-correlation energy of the system of non-interacting electrons with charge density $n(\boldsymbol{r})$. The exchange-correlation potential becomes

$$V_{xc}(\boldsymbol{r}) \approx \left[\frac{\mathrm{d}}{\mathrm{d}n}(n\epsilon_{xc}(n))\right]_{n=n(\boldsymbol{r})}. \tag{10}$$

Since the effective potential is a function of the charge density, the Kohn–Sham equations can be solved self-consistently until the densities at iterations i and $(i+1)$ are in agreement.

In the generalization of density functional theory to magnetic systems [27–32], the so-called spin density functional theory, one distinguishes between two types of electrons, namely the majority electrons ($\sigma = +$ or $\sigma = \uparrow$) and the minority electrons ($\sigma = -$ or $\sigma = \downarrow$) whose spin is in and opposite to the direction of magnetization, respectively. The two types of particles are represented by spin-dependent densities $n^+(\boldsymbol{r})$ and $n^-(\boldsymbol{r})$, leading accordingly to the following functional for the ground state energy:

$$E[n^+, n^-] = T[n] + \int \mathrm{d}^3r\, V_{\text{ext}}(\boldsymbol{r})n(\boldsymbol{r}) + U[n] + E_{xc}[n^+, n^-] \tag{11}$$

with a total density given by

$$n(\boldsymbol{r}) = n^{+}(\boldsymbol{r}) + n^{-}(\boldsymbol{r}) \tag{12}$$

and the magnetization density given by

$$m(\boldsymbol{r}) = n^{+}(\boldsymbol{r}) - n^{-}(\boldsymbol{r}). \tag{13}$$

Clearly, the ground state energy is a functional of both spin-dependent densities, $E[n^{+}, n^{-}]$. Using spin-dependent densities in terms of single-particle wavefunctions

$$n^{\sigma}(\boldsymbol{r}) = \sum_{k} |\varphi_{k}^{\sigma}(\boldsymbol{r})|^{2}, \qquad \sigma = (+, -) \tag{14}$$

the variation of the ground state energy yields the spin-dependent Kohn–Sham equations

$$\left[-\frac{\hbar^{2}}{2m}\frac{\partial^{2}}{\partial \boldsymbol{r}^{2}} + V^{\sigma}(\boldsymbol{r})\right]\varphi_{k}^{\sigma}(\boldsymbol{r}) = E_{k}^{\sigma}\varphi_{k}^{\sigma}(\boldsymbol{r}). \tag{15}$$

and, by analogy with the spin-independent case an effective though spin-dependent potential follows as

$$V^{\sigma} = V_{\text{ext}}(\boldsymbol{r}) + \int \mathrm{d}^{3}r'\, n(\boldsymbol{r}')\frac{\epsilon^{2}}{|\boldsymbol{r} - \boldsymbol{r}'|} + V_{xc}^{\sigma}(\boldsymbol{r}) \tag{16}$$

with

$$V_{xc}^{\sigma} = \frac{\delta E_{xc}}{\delta n^{\pm}(\boldsymbol{r})}.$$

Under local spin density approximation, the exchange-correlation energy [29,30] writes

$$E_{xc}[n^{+}, n^{-}] \approx \int \mathrm{d}^{3}r\, (n^{+}(\boldsymbol{r}) + n^{-}(\boldsymbol{r}))\epsilon_{xc}^{\text{hom}}(n^{+}(\boldsymbol{r}), n^{-}(\boldsymbol{r})) \tag{17}$$

and

$$V_{xc}^{\sigma} \approx \left[\frac{\partial}{\partial n^{\pm}}(n^{+} + n^{-})\epsilon_{xc}^{\text{hom}}(n^{+}, n^{-})\right]_{n^{\sigma} = n^{\sigma}(\boldsymbol{r})}. \tag{18}$$

Different approximations of the local density and the local spin density functional [28–30,33] have been used. They lead to variations within the error of the local density or spin density approximation itself.

2.2. The Green function

A variety of techniques can be utilized to solve the Kohn–Sham equations (6) and (15). One of these is the equivalent formulation in terms of a Green function

$$\left(-\frac{\hbar^{2}}{2m}\frac{\partial^{2}}{\partial \boldsymbol{r}^{2}} + V(\boldsymbol{r}) - E\right)G(\boldsymbol{r}, \boldsymbol{r}'; E) = -\delta(\boldsymbol{r} - \boldsymbol{r}') \tag{19}$$

and

$$\left(-\frac{\hbar^{2}}{2m}\frac{\partial^{2}}{\partial \boldsymbol{r}^{2}} + V^{\sigma}(\boldsymbol{r}) - E\right)G^{\sigma}(\boldsymbol{r}, \boldsymbol{r}'; E) = -\delta(\boldsymbol{r} - \boldsymbol{r}') \tag{20}$$

for spin-independent and spin-dependent systems, respectively. Not only does the Green function include the same information on the the electronic states of a translationally invariant system for a given potential $V(\boldsymbol{r})$ as the other available techniques, but it is especially appropriate for the treatment of non-translationally invariant systems such as, for example, impurity atoms in an otherwise perfect crystal, interfaces or surfaces.

The formulation of the Green function method was introduced by Dupree [14], Beeby [15] and Holzwarth [16]. It was further developed, refined and applied to real systems by Dederichs and Zeller [18,19], Terakura [34–36], Oppeneer and Lodder [37,38], Lehmann [17] and Mertig *et al* [20].

2.2.1. Muffin-tin approximation. The translationally invariant crystal potential

$$V(\boldsymbol{r}+\boldsymbol{R}_n) = V(\boldsymbol{r}) \tag{21}$$

where $\boldsymbol{R}_n$ is a lattice vector, is regarded as a superposition of local potentials of finite range [39,40]

$$V(\boldsymbol{r}) = \sum_n V_n(\boldsymbol{r}-\boldsymbol{R}_n). \tag{22}$$

For metals either spherical non-overlapping potentials V_n, so-called muffin-tin spheres, centred at lattice spaces with a region of constant potential in between or overlapping spheres, so-called atomic spheres, with no interstitial region between the spheres are chosen. The assumption of a muffin-tin form for the potential played an essential role for the early development of the Green function method. During recent years the Green function method was also extended to full potentials [41,42]. The calculations have shown that spherical potentials are sufficient in almost all cases and that the principal source of mistakes for total energy calculations results from the assumption of spherical charge densities.

2.2.2. The Green function of the unperturbed system. In a spectral representation, the Green function is expressed in terms of the eigenfunctions $\varphi_k^\sigma(\boldsymbol{r})$ of the Kohn–Sham operator

$$G^\sigma(\boldsymbol{r},\boldsymbol{r}',E) = \sum_k \frac{\varphi_k^\sigma(\boldsymbol{r})\varphi_k^\sigma(\boldsymbol{r}')^*}{E+\mathrm{i}\varepsilon-E_k^\sigma} \qquad \varepsilon \overset{\rightarrow}{>} 0 \tag{23}$$

where the poles are the eigenvalues E_k^σ of the Kohn–Sham operator. In view of the Dirac identity

$$\lim_{\varepsilon\to 0}\frac{1}{E-{E_k}^\sigma+\mathrm{i}\varepsilon} = \boldsymbol{P}\frac{1}{E-{E_k}^\sigma} - \mathrm{i}\pi\delta(E-{E_k}^\sigma), \tag{24}$$

($\boldsymbol{P}$ stands for the Cauchy principle part) the energy dependent spin density $n^\sigma(\boldsymbol{r},E)$ can be related to the imaginary part of the Green function [20]

$$n^\sigma(\boldsymbol{r},E) = \sum_k |\varphi_k^\sigma(\boldsymbol{r})|^2\delta(E-E_k^\sigma) = -\frac{1}{\pi}\mathrm{Im}\,G^\sigma(\boldsymbol{r},\boldsymbol{r};E). \tag{25}$$

The spin density then results from an integration with respect to energy over all occupied states

$$n^\sigma(\boldsymbol{r}) = -\frac{1}{\pi}\int_{-\infty}^{E_F}\mathrm{d}E\,\mathrm{Im}\,G^\sigma(\boldsymbol{r},\boldsymbol{r};E). \tag{26}$$

The sum of the spin densities determines the total charge density (equation (12)) whereas the magnetization density is given by the difference (equation (13)). The spin-dependent density of states writes

$$N^\sigma(E) = -\frac{1}{\pi}\int_{V_z}\mathrm{d}^3r\,\mathrm{Im}\,G^\sigma(\boldsymbol{r},\boldsymbol{r};E) \tag{27}$$

obtained by an spatial integration over the volume of the elementary cell V_z or in terms of the equivalent operator notation (27)

$$N^\sigma(E) = -\frac{1}{\pi}\mathrm{Im}\ \mathrm{Tr}\,G^\sigma(E) \tag{28}$$

by means of the trace of the Green function with respect to spatial dependence. Thus, the integrated density of states can be written as [43]

$$\mathcal{N}^\sigma(E) = \int_{-\infty}^{E}\mathrm{d}E'\,N^\sigma(E') = -\frac{1}{\pi}\mathrm{Im}\ \mathrm{Tr}\ln G^\sigma(E). \tag{29}$$

Then, $\mathcal{N}(E_F) = \mathcal{N}^+(E_F) + \mathcal{N}^-(E_F)$ and $M(E_F) = \mathcal{N}^+(E_F) - \mathcal{N}^-(E_F)$ represent the total number of electrons and the total magnetic moment of the system, respectively.

With the spatial dependence of the Green function expressed in terms of cell-centred coordinates $\boldsymbol{r} \to \boldsymbol{R}_n + \boldsymbol{r}$ and $\boldsymbol{r}' \to \boldsymbol{R}_{n'} + \boldsymbol{r}'$ whereby $\boldsymbol{r}$ and $\boldsymbol{r}'$ are restricted to the Wigner–Seitz cell, equation (19) becomes

$$\left(-\frac{\hbar^2}{2m}\frac{\partial^2}{\partial \boldsymbol{r}^2} + V_n^\sigma(\boldsymbol{r}) - E\right) G^\sigma(\boldsymbol{R}_n + \boldsymbol{r}; \boldsymbol{R}_{n'} + \boldsymbol{r}'; E) = -\delta_{nn'}\delta(\boldsymbol{r} - \boldsymbol{r}'). \quad (30)$$

For $\boldsymbol{R}_n \neq \boldsymbol{R}_{n'}$ and $\boldsymbol{r} \neq \boldsymbol{r}'$, the source term contained in the right-hand side of equation (30) vanishes and the Green function satisfies the homogeneous Schrödinger equation. Thus, G can be expressed in terms of the linearly independent regular and irregular solutions of the radial Schrödinger equation

$$R_{Ln}^\sigma(\boldsymbol{r}, E) = R_{ln}^\sigma(r, E) Y_L(\hat{\boldsymbol{r}}) \qquad \text{and} \qquad H_{Ln}^\sigma(\boldsymbol{r}, E) = H_{ln}^\sigma(r, E) Y_L(\hat{\boldsymbol{r}}) \quad (31)$$

with spherical potential $V_n^\sigma(\boldsymbol{r})$. $Y_L(\hat{\boldsymbol{r}})$ are real spherical harmonics with a shorthand notation L for angular momentum l and magnetic quantum number m and $\hat{\boldsymbol{r}} = \boldsymbol{r}/r$. The Green function becomes [44]

$$\begin{aligned} G^\sigma(\boldsymbol{R}_n + \boldsymbol{r}, \boldsymbol{R}_{n'} + \boldsymbol{r}'; E) &= \delta_{nn'}\frac{2m}{\hbar^2}\kappa \sum_L Y_L(\hat{\boldsymbol{r}}) R_{ln}^\sigma(r_<, E) H_{ln}^\sigma(r_>, E) Y_L(\hat{\boldsymbol{r}}') \\ &\quad + \sum_{LL'} Y_L(\hat{\boldsymbol{r}}) R_{ln}^\sigma(r, E) G_{LL'}^{nn'\sigma}(E) R_{l'n'}^\sigma(r', E) Y_{L'}(\hat{\boldsymbol{r}}') \end{aligned} \quad (32)$$

with $r_< = \min(r, r')$, $r_>$, $= \max(r, r')$ and $\kappa = \sqrt{\frac{2m}{\hbar^2}E}$.

The first term of equation (32) is the Green function of a single scattering potential V_n in free space which results from the source term of equation (30).

The second term, which consists of regular solutions only, satisfies the homogeneous Schrödinger equation. It should be noted that the so-called structural Green function $G_{LL'}^{nn'}(E)^\sigma$ accounts for all the multiple scattering processes between the muffin-tin potentials.

In the case of a superposition of identical potentials:

$$V^\sigma(\boldsymbol{r}) = \sum_n \mathring{V}^\sigma(\boldsymbol{R}_n + \boldsymbol{r}) \quad (33)$$

with the linearly independent solutions $\mathring{R}_l^\sigma(r, E)$ and $\mathring{H}_l^\sigma(r, E)$ of the radial Schrödinger equation with potential $\mathring{V}^\sigma(\boldsymbol{r})$ the Green function of the ideal crystal writes

$$\begin{aligned} \mathring{G}^\sigma(\boldsymbol{R}_n + \boldsymbol{r}, \boldsymbol{R}_{n'} + \boldsymbol{r}'; E) &= \delta_{nn'}\frac{2m}{\hbar^2}\kappa \sum_L Y_L(\hat{\boldsymbol{r}}) \mathring{R}_l^\sigma(r_<, E) \mathring{H}_l^\sigma(r_>, E) Y_L(\hat{\boldsymbol{r}}') \\ &\quad + \sum_{LL'} \mathring{R}_L^\sigma(\boldsymbol{r}, E) \mathring{G}_{LL'}^{nn'\sigma}(E) \mathring{R}_{L'}^\sigma(\boldsymbol{r}', E). \end{aligned} \quad (34)$$

It is worthwhile noticing that because of translational invariance, the structural Green function $\mathring{G}_{LL'}^{nn'\sigma}(E)$ depends on $\boldsymbol{R}_n - \boldsymbol{R}_{n'}$ only.

2.2.3. The Green function of the perturbed system. The Green function of the perturbed and the unperturbed system are related by a Dyson equation

$$G^\sigma = \mathring{G}^\sigma + \mathring{G}^\sigma \Delta V^\sigma G^\sigma \quad (35)$$

ΔV is the change brought about by the defect to the potential

$$\Delta V^\sigma(\boldsymbol{r}) = \sum_n \Delta V_n^\sigma(\boldsymbol{r}) = \sum_n V_n^\sigma(\boldsymbol{r}) - \mathring{V}^\sigma(\boldsymbol{r}). \quad (36)$$

The electronic structure of the perturbed system, that is, $n^\sigma(\boldsymbol{r}, E)$, $n^\sigma(\boldsymbol{r})$, $N^\sigma(E)$ (equations (25)–(29)), is entirely known once the Green function of the perturbed system (equation (35)) is calculated. Consequently, the impurity atom causes the following changes in spin density

$$\Delta n^\sigma(\boldsymbol{r}) = -\frac{1}{\pi}\int_{-\infty}^{E_F} \mathrm{d}E\, \mathrm{Im}\,[G^\sigma(\boldsymbol{r}, \boldsymbol{r}, E) - \mathring{G}^\sigma(\boldsymbol{r}, \boldsymbol{r}; E)], \tag{37}$$

the density of states

$$\Delta N^\sigma(E) = -\frac{1}{\pi}\int_{V_z} \mathrm{d}^3 r\, \mathrm{Im}\,[G^\sigma(\boldsymbol{r}, \boldsymbol{r}; E) - \mathring{G}^\sigma(\boldsymbol{r}, \boldsymbol{r}; E)] \tag{38}$$

the total number of occupied states

$$\Delta\mathcal{N}(E_F) = \Delta\mathcal{N}^+(E_F) + \Delta\mathcal{N}^-(E_F), \tag{39}$$

the magnetization

$$\Delta M(E_F) = \Delta\mathcal{N}^+(E_F) - \Delta\mathcal{N}^-(E_F) \tag{40}$$

where

$$\Delta\mathcal{N}^\sigma(E_F) = \int_{-\infty}^{E_F} \mathrm{d}E\, [N^\sigma(E) - \mathring{N}^\sigma(E)]. \tag{41}$$

Equation (35) can be rewritten with respect to cell-centred coordinates as

$$G^\sigma(\boldsymbol{R}_n + \boldsymbol{r}, \boldsymbol{R}_{n'} + \boldsymbol{r}'; E) = \mathring{G}^\sigma(\boldsymbol{R}_n + \boldsymbol{r}, \boldsymbol{R}_{n'} + \boldsymbol{r}'; E) + \sum_{n''}\int \mathrm{d}^3 r''\, \mathring{G}^\sigma(\boldsymbol{R}_n + \boldsymbol{r}, \boldsymbol{R}_{n''} + \boldsymbol{r}''; E)\Delta V^\sigma_{n''}(r'')G^\sigma(\boldsymbol{R}_{n''} + \boldsymbol{r}'', \boldsymbol{R}_{n'} + \boldsymbol{r}'; E). \tag{42}$$

Combining equation (42) with equations (32) and (34) yields an algebraic Dyson equation

$$G^{nn^\sigma}_{LL'}(E) = \mathring{G}^{nn'^\sigma}_{LL'}(E) + \sum_{L'',n''} \mathring{G}^{nn''^\sigma}_{LL''}(E)\Delta t^{n''^\sigma}_{l''}(E)G^{n''n'^\sigma}_{L''L'}(E), \tag{43}$$

which relates the structural Green function of the defect $G^{nn'^\sigma}_{LL'}(E)$ to that of the ideal host $\mathring{G}^{nn'^\sigma}_{LL'}(E)$. It should be noted that, instead of the difference of potentials, equation (43) involves the difference between single-site transition matrices Δt^n_l [20]

$$\Delta t^{n^\sigma}_l(E) = t^{n^\sigma}_l(E) - \mathring{t}^\sigma_l(E) \tag{44}$$

with

$$t^{n^\sigma}_l(E) = -\frac{\hbar^2}{2m\kappa}\sin\eta^{n^\sigma}_l(E)\mathrm{e}^{\mathrm{i}\eta^{n^\sigma}_l}(E). \tag{45}$$

$\eta^{n^\sigma}_l(E)$ are the scattering phase shifts of the potential V^σ_n.

The rank of the algebraic Dyson equation is determined by the extension of the defect, that is, the number n of perturbed neighbouring potentials.

2.2.4. Perturbed Bloch waves. The single-particle wavefunction of a translationally invariant system is a Bloch wave whose angular momentum expansion at the cell centre $\boldsymbol{R}_n$ writes

$$\mathring{\varphi}_k(\boldsymbol{R}_n + \boldsymbol{r}) = \frac{1}{\sqrt{V}}\sum_L \mathring{c}^n_L(k)\mathring{R}^\sigma_L(\boldsymbol{r}, E) \tag{46}$$

with k characterizing the electronic state via the set of quantities $(\boldsymbol{k}, \nu, \sigma)$ where $\boldsymbol{k}$ is the Bloch vector, ν the band index and σ its spin. The coefficients $\mathring{c}_L^n(k)$ are a contracted notation between Bloch factors and expansion coefficients $\mathring{c}_L(\boldsymbol{k})$

$$\mathring{c}_L^n(k) = \mathrm{e}^{\mathrm{i}\boldsymbol{k}\boldsymbol{R}_n}\mathring{c}_L(k). \tag{47}$$

By analogy with equation (46), a perturbed Bloch wave can be defined in terms of radial eigenfunctions as

$$\varphi_k(\boldsymbol{R}_n + \boldsymbol{r}) = \frac{1}{\sqrt{V}}\sum_L c_L^n(k) R_L^{n^\sigma}(\boldsymbol{r}, E) \tag{48}$$

which represents an angular momentum expansion of the wavefunction in the cell centred at $\boldsymbol{R}_n$ of the perturbed crystal. The perturbed Bloch wave is a solution of the so-called Lippmann–Schwinger equation

$$\varphi_k(\boldsymbol{R}_n + \boldsymbol{r}) = \mathring{\varphi}_k(\boldsymbol{R}_n + \boldsymbol{r}) + \sum_{n'}\int \mathrm{d}^3r'\,\mathring{G}^\sigma(\boldsymbol{R}_n + \boldsymbol{r}, \boldsymbol{R}_{n'} + \boldsymbol{r}', E)\Delta V_{n'}(\boldsymbol{r}')\varphi_k(\boldsymbol{R}_{n'} + \boldsymbol{r}') \tag{49}$$

obtained by projecting onto φ_k the combination between equations (23) and (35). $\mathring{G}^\sigma$ is the Green function of the ideal system (see also sections 2.2.2 and 2.2.3). With equations (46) and (48), equation (49) can be expressed as

$$c_L^n(k) = \mathring{c}_L^n(k) + \sum_{n'L'}\mathring{G}_{LL'}^{nn'^\sigma}(E)\Delta t_{l'}^{n'^\sigma}(E)c_{L'}^{n'}(k). \tag{50}$$

The expansion coefficients of the perturbed Bloch wave can be expressed in terms of the expansion coefficients of the unperturbed Bloch wave

$$c_L^n(k) = \sum_{n'L'} D_{LL'}^{nn'^\sigma}(E)\mathring{c}_{L'}^{n'}(k) \tag{51}$$

where the matrix D writes

$$D_{LL'}^{nn'^\sigma}(E) = [(1 - \mathring{G}^\sigma(E)\Delta t^\sigma(E))^{-1}]_{LL'}^{nn'}, \tag{52}$$

which by means of equation (35), can also be expressed in terms of the perturbed Green function

$$D_{LL'}^{nn'^\sigma}(E) = [1 + G^\sigma(E)\Delta t^\sigma(E)]_{LL'}^{nn'}. \tag{53}$$

This representation (equation (53)) will be used in what follows.

2.2.5. The T matrix. Consider the scattering of an unperturbed Bloch wave by a perturbation ΔV (equation (36) and figure 1) during which both spin and energy are conserved. This process can be expressed in terms of the T matrix

$$T_{kk'} = \frac{1}{V}\int \mathrm{d}^3r\,\mathring{\varphi}_k(\boldsymbol{r})\Delta V^\sigma(\boldsymbol{r})\varphi_{k'}(\boldsymbol{r}) \tag{54}$$

which, combined with equation (46) and (48), becomes

$$T_{kk'} = \frac{1}{V}\sum_{nL}\mathring{c}_L^{n^*}(k)\Delta_l^{n^\sigma}(E)c_L^n(k') \tag{55}$$

with

$$\Delta_l^{n^\sigma}(E) = \mathrm{e}^{-2\mathrm{i}\mathring{\eta}_l^\sigma(E)}\Delta t_l^{n^\sigma}(E). \tag{56}$$

By use of equation (51), T transforms into

$$T_{kk'} = \frac{1}{V}\sum_{nn'LL'}\mathring{c}_L^n(k)T_{LL'}^{nn'^\sigma}(E)\mathring{c}_{L'}^{n'}(k'), \tag{57}$$

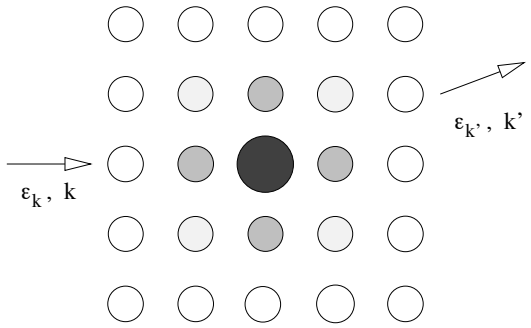

Figure 1. Scattering of a Bloch wave at a cluster of perturbed potentials.

with

$$T_{LL'}^{nn'\sigma} = \mathrm{e}^{-2\mathrm{i}\mathring{\eta}_l^\sigma(E)}\Delta t_l^{n^\sigma}(1 + G_{LL'}^{nn'\sigma}(E)\Delta t_{l'}^{n'^\sigma}(E)). \tag{58}$$

$\mathring{\eta}_l^\sigma$ are the scattering phase shifts of the unperturbed potential and $\Delta t_l^{n^\sigma}$ are the differences of the single-site t matrices of the perturbed and unperturbed potentials (equation (44)). By contrast, the structural Green function $G_{LL'}^{nn'\sigma}$ of the perturbed system contains all the information about multiple scattering processes between the potential spheres. The T matrix will be used in the following representation

$$T_{kk'} = \frac{1}{V}\sum_{nL}\mathring{c}_L^n(k)Q_L^n(k') \tag{59}$$

where the generalized wavefunction coefficients $Q_L^n(k)$ write

$$Q_L^n(k) = \sum_{n'L'} T_{LL'}^{nn'\sigma}\mathring{c}_{L'}^{n'}(k). \tag{60}$$

2.2.6. The microscopic transition probability. In the limit of non-interacting scattering centres, the microscopic transition probability for an electron to scatter from a state k to a state k', is given by Fermi's golden rule

$$P_{kk'} = \frac{2\pi}{\hbar}cN|T_{kk'}|^2\delta(E_k - E_{k'}) \tag{61}$$

where c is the concentration of defects, cN the number of perturbed atoms in the system. In fact, the relaxation time

$$\tau_k^{-1} = \sum_{k'} P_{kk'} \tag{62}$$

characterizes the scattering process most meaningfully for it represents the time that an electron stays in the state k until the next scattering event. By virtue of the optical theorem

$$\sum_{k'}|T_{kk'}|^2\delta(E_{k'} - E_k) = -\frac{1}{\pi}\mathrm{Im}\,T_{kk} \tag{63}$$

the relaxation time is expressed by the imaginary part of the diagonal elements of T

$$\tau_k^{-1} = -\frac{2}{\hbar}cN\mathrm{Im}\,T_{kk}. \tag{64}$$

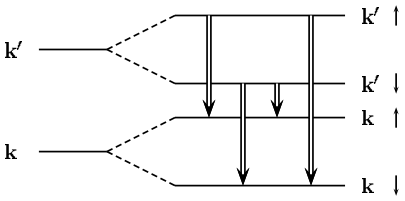

Figure 2. Spin-dependent scattering in ferromagnetic systems.

In ferromagnetic systems the scattering probability $P_{kk'}$ contains in fact four components depending upon the spin-quantum numbers before and after scattering (figure 2)

$$P_{kk'}^{\sigma\sigma'} = \begin{pmatrix} P_{kk'}^{\uparrow\uparrow} & P_{kk'}^{\uparrow\downarrow} \\ P_{kk'}^{\downarrow\uparrow} & P_{kk'}^{\downarrow\downarrow} \end{pmatrix} \tag{65}$$

thus k now stands only for $(\boldsymbol{k}, \nu)$. Although, there are several mechanisms of spin mixing we restrict our consideration to potential scattering, that is, the diagonal elements of equation (65) only. The non-diagonal spin mixing elements result principally from the scattering by spin waves [45] or from collisions between spin-up and spin-down electrons [46], both mechanisms cease to operate at 0 K. But there are also residual spin-mixing terms. Spin-flip can occur upon scattering by impurities via spin–orbit coupling, but the corresponding cross section is about two orders of magnitude smaller than that of the spin-conserving scattering potential [47]. At 0 K spin-mixing can also result from the combined action of the internal magnetic induction and the spin–orbit coupling. This term is neglected without justification.

The microscopic transition probability can be transformed by means of equation (59) into

$$P_{kk'} = P_0 \delta(E_k - E_{k'}) \sum_{nn'LL'} Q_L^{n^*}(k) Q_{L'}^{n'}(k) \mathring{c}_L^n(k') \mathring{c}_{L'}^{n'^*}(k') \tag{66}$$

with $P_0 = c(\hbar^2/2mE_F)$.

3. Transport theory

This part concentrates on a first principle description of transport properties in the frame of electronic structure methods. The application of transport theory to dilute alloys will be presented in a subsequent section.

3.1. Macroscopic transport coefficients

Assuming linear response of the considered system to the influence of any external fields, we shall always find that the densities of the electrical current $\boldsymbol{j}$ and of the thermal current $\boldsymbol{q}$ are linear functions of the electric field $\boldsymbol{E}$ and of the temperature gradient along the sample ∇T

$$\boldsymbol{j} = \hat{L}_{EE}\boldsymbol{E} + \hat{L}_{ET}\nabla T, \tag{67}$$

$$\boldsymbol{q} = \hat{L}_{TE}\boldsymbol{E} + \hat{L}_{TT}\nabla T. \tag{68}$$

All the generalized transport coefficients $\hat{L}$ are tensors which reduce to scalars L in case of cubic systems. The generalized transport coefficients are however not observed directly. They are combinations of measured transport properties as follows [48].

Electrical conductivity $\hat{\sigma}$. Given the temperature, an electric current takes place upon application of an electric field. Under this conditions equation (67) becomes

$$\boldsymbol{j} = \hat{L}_{EE}\boldsymbol{E}. \tag{69}$$

Comparison with Ohm's law

$$\boldsymbol{j} = \hat{\sigma}\boldsymbol{E} \tag{70}$$

leads to

$$\hat{\sigma} = \hat{L}_{EE}, \tag{71}$$

where $\hat{\sigma}$ is the electrical conductivity. The electrical resistivity is given by $\hat{\rho} = \hat{\sigma}^{-1}$.

Thermal conductivity $\hat{\kappa}$. The specimen is electrically insulated to prevent any electric current flowing through it. A thermal gradient is maintained, and the flux of heat measured. Under these conditions equations (67) and (68) reduce to

$$\boldsymbol{E} = -\hat{L}_{EE}^{-1}\hat{L}_{ET}\nabla T, \tag{72}$$

$$\boldsymbol{q} = (\hat{L}_{TT} - \hat{L}_{TE}\hat{L}_{EE}^{-1}\hat{L}_{ET})\nabla T. \tag{73}$$

In view of the empirical relation

$$\boldsymbol{q} = -\hat{\kappa}\nabla T \tag{74}$$

the thermal conductivity is written

$$\hat{\kappa} = \hat{L}_{TE}\hat{L}_{EE}^{-1}\hat{L}_{ET} - \hat{L}_{TT}. \tag{75}$$

What happens is that, in order to stop the flow of electric current, carried by the flux of heat, an electric field has to build up along the specimen. This field slightly reduces the thermal current so that the thermal conductivity is not simply the coefficient $-\hat{L}_{TT}$.

Thermopower S. If instead of the thermal current the electric field caused by a thermal gradient is measured for the same experimental conditions

$$\boldsymbol{E} = S\nabla T \tag{76}$$

we obtain the absolute thermopower of a metal

$$S = -\hat{L}_{EE}^{-1}\hat{L}_{ET}. \tag{77}$$

Peltier coefficient Π. Using the conditions under which the electrical conductivity was measured there will also be a thermal current associated which is proportional to the electric field

$$\boldsymbol{q} = \Pi\boldsymbol{j}. \tag{78}$$

Combined with equations (67) and (68), equation (78) yields the following expression of the Peltier coefficient

$$\Pi = \hat{L}_{TE}\hat{L}_{EE}^{-1}. \tag{79}$$

From these four measurements, the generalized transport coefficients which relate the currents to the fields (equations (67) and (68)), can be entirely determined.

Kelvin–Onsager relation. The thermopower and the Peltier coefficient are related by

$$S = \Pi T \tag{80}$$

which implies the following dependence of $\hat{L}_{ET}$ upon $\hat{L}_{TE}$

$$\hat{L}_{ET} = -\hat{L}_{TE}/T. \tag{81}$$

Wiedemann–Franz law. As long as the following approximation for the thermal conductivity holds (see equation (75))

$$\kappa \approx -\hat{L}_{TT} \tag{82}$$

the thermal conductivity remains proportional to the electrical conductivity

$$\kappa \approx L_0 \sigma \tag{83}$$

where L_0 is the Lorentz number.

In case of metals the externally applied electric field amounts to

$$E \approx \frac{j}{\sigma} \sim 10^{-2} \frac{V}{m} \tag{84}$$

while the external magnetic field is in the range

$$B = 10\text{–}100 \text{ T}. \tag{85}$$

On the other hand, an order of magnitude for the atomic field is given by

$$E_0 \approx \frac{e}{4\pi\epsilon_0 a_0^2} \sim 10^{11} \frac{V}{m} \tag{86}$$

where a_0 is the Bohr radius, while the atomic magnetic field scales with

$$B_0 \approx \frac{E_0}{v_F} \sim \frac{\hbar}{e a_0} \sim 10^5 \text{ T}, \tag{87}$$

where v_F is a typical Fermi velocity. Hence it should be kept in mind that since external fields are by several orders of magnitude smaller than the atomic electric and magnetic fields, the electronic structure of the system is essentially unchanged during the above measurements of transport coefficients (Landau levels are neglected for the consideration of the conductivity).

3.2. Boltzmann equation

For the description of transport properties of a metallic system from a microscopic level, two options are in general available. On the one hand, the transport coefficients can be treated in a fully quantum mechanical manner based on Kubo's linear response formalism [5], as exemplified by the *ab initio* treatments of transport coefficients of disordered alloys [9, 49]. Unfortunately, the method does not allow for a clear understanding of the microscopic processes which lay behind the macroscopic transport coefficient.

On the other hand, one may take advantage of the quasi-classical approach of transport founded on the Boltzmann equation. This description accounts for the microscopic origin of the transport coefficients very satisfactorily and it is valid every time the mean free path is simultaneously small relative to the macroscopic dimension of the system and large as compared to the lattice parameter.

Boltzmann theory assumes the existence of a distribution function $f_k(\boldsymbol{r})$ which measures the number of carriers in the state k in the neighbourhood of $\boldsymbol{r}$. This distribution function

changes through diffusion of charge carriers, under the influence of external fields and due to scattering, giving rise to a net rate of change

$$\frac{\partial f_k(\boldsymbol{r})}{\partial t}$$

which should vanish in the steady state. The resulting condition is the Boltzmann equation

$$\left(\frac{\partial f_k(\boldsymbol{r})}{\partial t}\right) + \left(\frac{\partial f_k(\boldsymbol{r})}{\partial t}\right)_{\text{diffusion}} + \left(\frac{\partial f_k(\boldsymbol{r})}{\partial t}\right)_{\text{field}} = \left(\frac{\partial f_k(\boldsymbol{r})}{\partial t}\right)_{\text{scattering}} \tag{88}$$

where the terms at the left-hand side account for changes of the distribution function due to an explicit time dependence, due to diffusion and due to the influence of external fields. All these changes have to be in equilibrium with the changes of the distribution function through scattering.

We restrict the following considerations to a homogeneous external electric field $\boldsymbol{E}$. Equation (88) thus reduces to

$$e\left(\frac{\partial f_k^0}{\partial E_k}\right)\boldsymbol{v}_k\boldsymbol{E} = \left(\frac{\partial f_k}{\partial t}\right)_{\text{scattering}} \tag{89}$$

where $\boldsymbol{v}_k$ is the velocity of the electrons which can be obtained from the single-particle energies of the considered system

$$\boldsymbol{v}_k = \frac{1}{\hbar}\frac{\partial E_k}{\partial \boldsymbol{k}}. \tag{90}$$

f_k^0 is the Fermi–Dirac distribution function

$$f_k^0 = \frac{1}{\mathrm{e}^{(E_k - E_F)/k_B T} + 1} \tag{91}$$

at 0 K. k_B is Boltzmann's constant. The local change of charge carriers due to elastic scattering of independent particles can be related to the microscopic scattering probability by

$$\left(\frac{\partial f_k}{\partial t}\right)_{\text{scattering}} = \sum_{k'}[f_{k'}(1 - f_k)P_{k'k} - (1 - f_{k'})f_k P_{kk'}]. \tag{92}$$

The first term in equation (92) characterizes the scattering of electrons from occupied states k' into an unoccupied state k (scattering-in term) while the second term characterizes the reverse process, the scattering of an electron from an occupied state k into unoccupied states k' (scattering-out term). We separate f_k into two parts

$$f_k = f_k^0 + g_k, \tag{93}$$

where the deviations g_k from the equilibrium distribution function are assumed to be modest under a small external electric field $\boldsymbol{E}$. According to the principle of microscopic reversibility

$$P_{kk'} = P_{k'k} \tag{94}$$

and in view of equation (93) the ansatz for the local change of charge carriers (equation (92)) simplifies to

$$\left(\frac{\partial f_k}{\partial t}\right)_{\text{scattering}} = \sum_{k'} P_{kk'}(g_{k'} - g_k). \tag{95}$$

Assuming a linear response for the deviations of the electron distribution function means $g_k \sim |\boldsymbol{E}|$, hence we make the ansatz

$$g_k = -e\left(\frac{\partial f_k^0}{\partial E_k}\right)\boldsymbol{\lambda}_k\boldsymbol{E}, \tag{96}$$

where $\boldsymbol{\lambda}_k$ is the vector mean free path. The amount of the vector mean free path is the usual mean free path known from text books and measures the path of the electron between two successive scattering events. With equations (95) and (96) the Boltzmann equation (89) can be transformed into

$$\boldsymbol{\lambda}_k = \tau_k \left[\boldsymbol{v}_k + \sum_{k'} P_{kk'} \boldsymbol{\lambda}_{k'} \right]. \tag{97}$$

τ_k is the relaxation time for electron impurity scattering introduced by equation (62). In non-magnetic systems equation (97) is an integral equation from which the vector mean free path $\boldsymbol{\lambda}_k$ ($k = (\boldsymbol{k}, \nu)$) can be determined. In ferromagnetic systems ($k = (\boldsymbol{k}, \nu, \sigma)$) and in view of equation (65), the Boltzmann equation becomes a system of coupled integral equations which decouples if spin-flip scattering processes are ignored. Integration is performed over the anisotropic Fermi surface of the system under consideration.

The current density is written

$$\boldsymbol{j} = e \sum_k f_k \boldsymbol{v}_k \tag{98}$$

which is merely the product of charge density and velocity of charge carriers. The crystal volume is set to unity. Combining equations (93), (96) and (98) and comparing that to Ohm's law (equation (70)) yields the conductivity tensor $\hat{\sigma}$

$$\sigma_{ij} = e^2 \sum_k \delta(E_k - E_F) v_{k_i} \lambda_{k_j} \tag{99}$$

where the index i and j refer to the components along Cartesian coordinates. If cubic systems are considered $\sigma_{ij} = \sigma \delta_{ij}$. A factor of two will appear when considering the spin quantum number explicitly in non-magnetic systems. In ferromagnetic systems, the conductivity is usually split into spin-dependent contributions

$$(\rho^\sigma)^{-1}_{ij} = \sigma^\sigma_{ij} = e^2 \sum_k \delta(E_k - E_F) v^\sigma_{k_i} \lambda^\sigma_{k_j} \tag{100}$$

where $\hat{\sigma}^\uparrow$ and $\hat{\sigma}^\downarrow$ stand for the majority and the minority electrons, respectively and $k = (\boldsymbol{k}, \nu)$. Since the currents are in parallel (figure 3) [50] the total conductivity for cubic systems becomes

$$\sigma = \sigma^\uparrow + \sigma^\downarrow \qquad \text{with} \quad \hat{\sigma}^\sigma_{ij} = \sigma^\sigma \delta_{ij}, \tag{101}$$

which can be written equivalently in terms of the resistivities

$$\rho = \frac{\rho^\uparrow \rho^\downarrow}{\rho^\uparrow + \rho^\downarrow} \qquad \text{with} \quad \hat{\rho}^\sigma_{ij} = \rho^\sigma \delta_{ij}. \tag{102}$$

The spin anisotropy ratio

$$\alpha = \sigma^\uparrow / \sigma^\downarrow = \rho^\downarrow / \rho^\uparrow \tag{103}$$

is usually introduced to account for the individual contributions of the majority and minority electrons to the transport properties.

3.2.1. Exact solution. Using the special structure of the microscopic transition probability (equation (66)) the linearized Boltzmann equation can be transformed into

$$\boldsymbol{\lambda}^\sigma_k = \tau^\sigma_k \left[\boldsymbol{v}^\sigma_k + P_0 \sum_{nn'LL'} Q^{n\sigma^*}_L(k) Q^{n'\sigma}_{L'}(k) \Xi^{nn'\sigma}_{LL'} \right] \tag{104}$$

where the Fermi surface integral writes

$$\Xi^{nn'\sigma}_{LL'} = \sum_{k'} \delta(E_k - E_{k'}) \mathring{c}^{n\sigma}_L(k') \mathring{c}^{n'\sigma^*}_{L'}(k') \boldsymbol{\lambda}^\sigma_{k'}. \tag{105}$$

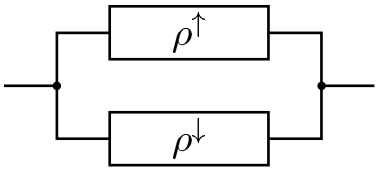

Figure 3. Total resistivity within the two-current model.

The Boltzmann equation (equations (104) and (105)) can, in general, be solved exactly since the integral kernel is degenerated [51], that is, the transition probability can be separated into terms that depend on k or on k'.

This idea has been implemented for a strongly localized point defect, that is, $n = n' = 1$ and applied for non-magnetic dilute alloys [8]. In the case of a perturbed cluster, an algebraic set of rank $R = (L \times L' \times n \times n')^2$ has to be solved instead of the integral equation. However, the exact solution becomes rapidly untractable numerically. For example, angular momenta up to $l = 3$ and 13 perturbed atoms in the cluster $R = (16 \times 16 \times 13 \times 13)^2 \widetilde{=} 2 \times 10^9$ are clearly too large for a numerical treatment.

Since the numerical solution of the problem is highly complicated several approximations have been developed which are discussed in the following.

3.2.2. Iterative solution. Since solving the Boltzmann equation (equations (104) and (105)) proves to be too large for a numerical treatment an iteration scheme was proposed by Coleridge [52]. It was later implemented by van Ek and Lodder [11] and by Mertig *et al* [12] for non-magnetic and magnetic systems, respectively. Several expressions have been tried to serve as a starting value in the iteration, such as the relaxation time approximation

$$\boldsymbol{\lambda}_k^{\sigma^0} = \tau_k^\sigma \boldsymbol{v}_k^\sigma \tag{106}$$

or the Ziman approximation

$$\boldsymbol{\lambda}_k^{\sigma\,Zi} = v_k^\sigma \frac{1}{\sum_{k'} \delta(E_k - E_{k'})(1 - \boldsymbol{v}_k^\sigma \boldsymbol{v}_{k'}^\sigma) P_{kk'}^\sigma} \tag{107}$$

and the degenerate kernel solution for the single-site case (see section 3.2.1). In all cases convergence was achieved without significantly different convergence rates. The mean free paths utilized were assumed to be converged if for all points on the Fermi surface the largest relative change in $\boldsymbol{\lambda}_k^\sigma$ between two subsequent iterations, i and $(i + 1)$, was less than 10^{-5}

$$\max \frac{||\boldsymbol{\lambda}_k^\sigma(i+1) - \boldsymbol{\lambda}_k^\sigma(i)||}{||\boldsymbol{\lambda}_k^\sigma(i)||} < 10^{-5}. \tag{108}$$

This criterion was met within ten iterations for all systems with $\rho \geqslant 1\ \mu\Omega$ cm/at%.

This method is nonetheless numerically extremely expensive, especially when the impurity cluster gets larger or when the Fermi surface becomes complicated. This is why a method combining iteration and a variational solution of the Boltzmann equation has been developed, which has greatly reduced the numerical effort as is shown in the next section.

3.2.3. Variational solution. From equations (89) and (95), the Boltzmann equation can be expressed in an abstract form as [48]

$$X = P\phi. \tag{109}$$

X is a known function which, in practice, depends on the external field via

$$X = e\frac{(\partial f_k^0)}{\partial E_k}\boldsymbol{v}_k\boldsymbol{E} \tag{110}$$

and P is the scattering operator. The problem is to find ϕ

$$P\phi = \sum_{k'} P_{kk'}(g_{k'} - g_k). \tag{111}$$

Let the inner product of two functions be

$$\langle\phi, \psi\rangle = \sum_k \phi(k)\psi(k). \tag{112}$$

and note that

$$\langle\phi, P\phi\rangle = \langle\phi, X\rangle. \tag{113}$$

The scattering operator is obviously linear, symmetric (see also equation (94)) and positive definite, because it is a measure of a probability. Hence

$$\langle\phi, P\phi\rangle \geqslant 0 \tag{114}$$

holds. The variational principle states that, of all functions which satisfy this condition (113), the solution of the integral equation is that which gives the quantity $\langle\phi, P\phi\rangle$ its maximum value. Several equivalent formulations are available for this theorem. For example, the solution of the integral equation will give the expression

$$\frac{\langle\phi, P\phi\rangle}{\{\langle\phi, X\rangle\}^2} \tag{115}$$

its minimum value, which coincides with the electrical resistivity in terms of the variational function [48]. Thus, the electrical resistivity is the extremal value of equation (115). If, instead of ϕ, we make use of the vector mean free path $\boldsymbol{\lambda}_k$ equation (113) can be transformed into

$$\langle\boldsymbol{\lambda}, P\boldsymbol{\lambda}\rangle = \langle\boldsymbol{\lambda}, \boldsymbol{v}\rangle. \tag{116}$$

Introducing the following trial function

$$\boldsymbol{\lambda}_k^{\text{trial}} = \sum_{i=1}^{N} \lambda^i \boldsymbol{\lambda}_k^i, \tag{117}$$

which is constructed on the solutions $\boldsymbol{\lambda}_k^i = \boldsymbol{\lambda}_k(i)$ of the first N iterations (section 3.2.2), equation (116) becomes

$$\sum_i \lambda^i v^i = \sum_{ij} \lambda^i \lambda^j P^{ij} \tag{118}$$

where

$$v^i = \langle\boldsymbol{\lambda}^i, \boldsymbol{v}\rangle \qquad \text{and} \qquad P^{ij} = \langle\boldsymbol{\lambda}^i, P\boldsymbol{\lambda}^j\rangle \tag{119}$$

are Fermi surface integrals. The variational principle then implies that the parameters $\boldsymbol{\lambda}^i$ should satisfy the algebraic set N^2 equations

$$v^i = \sum_j P^{ij}\lambda^j. \tag{120}$$

Since the trial functions are chosen to be strongly adapted to the problem, we are able to construct variational solutions. The numerical effort to get the variational solution is equivalent to the $(N + 1)$th iteration.

3.2.4. Relaxation time approximation. Because it is difficult to solve the linearized Boltzmann equation (equation (97)) numerically, several approximations have been introduced. In fact, the vector mean free path $\boldsymbol{\lambda}_k$ and the velocity $\boldsymbol{v}_k$ depend on each other via a tensorial relation which expresses the fact that, upon scattering, an electron can change direction and amount of its velocity. It should be noted that in relaxation time approximation, the scattering-in terms—here the second terms of the right-hand side of equation (97)—are ignored. We then obtain

$$\boldsymbol{\lambda}_k = \tau_k \boldsymbol{v}_k. \tag{121}$$

Clearly, the scattering process is no more fully taken into account since the analysis is restricted to scattering in direction of the velocity.

The next easiest approximation consists in neglecting the state dependence of the relaxation time. A Fermi surface average

$$\boldsymbol{\lambda}_k = \langle \tau_k \rangle \boldsymbol{v}_k \tag{122}$$

is substituted to τ_k, with the average defined as

$$\langle \tau_k \rangle = \frac{\sum_k \delta(E_k - E_F)\tau_k}{\sum_k \delta(E_k - E_F)}. \tag{123}$$

What occurs under this approximation is that the electrons are assumed to undergo the same scattering in all states k. If the conductivity of free electrons is calculated under the approximation (equation (122)) the expression

$$\sigma = \frac{ne^2\tau}{m} \tag{124}$$

is obtained. This is a standard result which is currently applied to all metallic systems without any consideration of the anisotropy of electronic structure.

The accuracy of the different approximations strongly depends upon the anisotropy of scattering. When the inversion symmetry of the Bravais lattice is not affected by the defect, the microscopic scattering probability obeys the following symmetry relation

$$P_{kk'} = P_{-k-k'} \tag{125}$$

which in turn implies

$$\boldsymbol{\lambda}_{-k'} = -\boldsymbol{\lambda}_{k'}. \tag{126}$$

Obviously, the scattering-in term can be transformed into

$$\begin{aligned} \sum_{k'} P_{kk'}\boldsymbol{\lambda}_{k'} &= \sum_{k'} \tfrac{1}{2}(P_{kk'}\boldsymbol{\lambda}_{k'} + P_{k-k'}\boldsymbol{\lambda}_{-k'}) \\ &= \sum_{k'} \tfrac{1}{2}(P_{kk'} - P_{k-k'})\boldsymbol{\lambda}_{k'} \end{aligned} \tag{127}$$

and is determined by the anti-symmetric part of the scattering operator

$$P^a_{kk'} = \tfrac{1}{2}(P_{kk'} - P_{k-k'}). \tag{128}$$

The lifetime, however, is related to the symmetric part of this operator

$$P^s_{kk'} = \tfrac{1}{2}(P_{kk'} + P_{k-k'}). \tag{129}$$

The relaxation time approximation is sufficient as long as the scattering probability for scattering from k into k' is equal to that from k into $-k'$ (figure 4), which is fulfilled for isotropic scattering. The approximation is however invalid in situations of strongly anisotropic scattering, as is the case of pronounced forward or backward scattering.

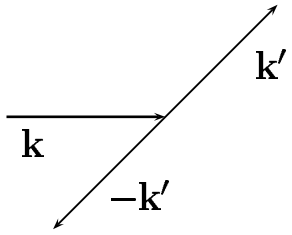

Figure 4. Symmetry of scattering probabilities.

3.2.5. Single-site approximation. Another common approximation for the solution of the Boltzmann equation is the so-called single-site approximation. Within this approximation all backscattering contributions from the crystalline environment of the scattering centre are neglected in the transition matrix (equations (55) and (58)). The resulting scattering matrix is the so-called single-site transition matrix

$$t_{kk'} = \frac{1}{V} \sum_{nn'LL'} \mathring{c}_L^{n^*}(k) \Delta_l^{n^\sigma}(E) \mathring{c}_L^{n}(k') \tag{130}$$

which enters the microscopic transition probability (equation (61)).

4. Residual resistivity

Concerning the transport properties, resistivity is one of the most fundamental properties of a metallic system. If the resistivity is investigated at extremely low temperatures the so-called residual resistivity is obtained. Residual resistivity is a fingerprint of a metallic system. Consequently, a large variety of highly precise experimental data exists.

The origin of residual resistivity in crystalline systems are lattice imperfections, as impurities and interstitials, dislocations, stacking faults and grain boundaries or chemical disorder in substitutional alloys. The theoretical investigations presented in the following section will give a detailed review of the microscopic origin of residual resistivity in dilute alloys.

4.1. Computational details

The *ab initio* treatment of transport properties is based on a highly sophisticated calculation of the electronic structure of dilute alloys. The computational methods to investigate the electronic structure of dilute alloys starting from density functional theory using the Green function technique (see section 3) have been refined over the last decade. The success of this development is characterized by an interplay of new methodical techniques and computer power. This section is a short summary of numerical details of the calculations.

A basic ingredient of all the calculations are the self-consistent potentials of the host material which are taken from Moruzzi *et al* [30]. The bandstructure was calculated by means of the so-called KKR (Korringa, Kohn and Rostoker) method [53, 54]. Within the KKR equations an angular momentum truncation at $l_{\max} = 4$ was used.

The imaginary part of the structural Green function was generated within the same KKR method by means of a Brillouin zone integration using the tetrahedron method [55, 56]. The real part of the Green function was calculated by a Hilbert transformation [56] with a truncation energy of 2.0 Ryd.

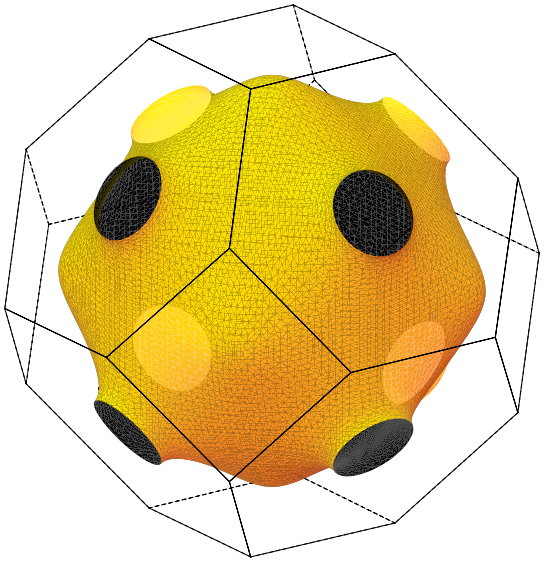

Figure 5. Topology of a Cu Fermi surface (see http://www.phy.tu-dresden.de/∼fermisur).

The self-consistent impurity calculations are performed within the frame of density functional theory [23, 24] using the local spin-density approximation as proposed by von Barth and Hedin [29] with parameters as chosen by Moruzzi *et al* [30]. To obtain the Green function of the perturbed system the algebraic Dyson equation is solved. The dimension of this equation is made finite by truncating the angular momentum expansion at $l = 3$ and by assuming potential perturbations only at the impurity site and at the first shells of atoms around the impurity.

The necessary Fermi surface integrations were performed with a modified tetrahedron method [20, 57].

4.2. Non-magnetic systems

The formalism of an *ab initio* calculation of residual resistivity was first applied to dilute noble metal alloys. For these systems a large variety of highly precise experimental data has already existed for a long time. General trends with respect to the impurity atom, like Linde's rule or the period effect, have been observed for sp defects in noble metals. The transport properties of transition metal impurities in noble metal hosts have been elucidated by the concept of resonance scattering at a virtual bound state.

4.2.1. Electronic structure of noble metals. Now, if we want to understand the microscopic processes behind the general trends for the residual resistivities we should concentrate our attention on the electronic states at the Fermi level since they determine the conductivity (equation (99)). The anisotropic electronic properties are the source of specific differences between the metallic systems whereby the Fermi surface acts as visiting card.

The electronic structure of noble metals is characterized by a fully occupied d band with strong hybridization between s and d states. This behaviour is reflected in the Fermi surface topology which is no longer a simple free electron sphere but exhibits characteristic necks (figure 5). Besides the Fermi surface topology Fermi velocities are an important input to

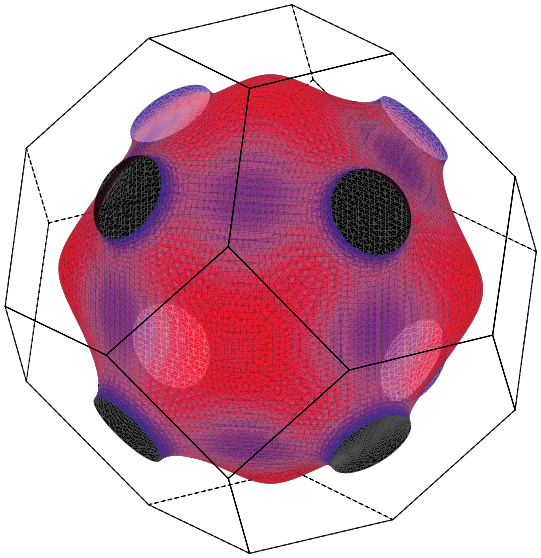

Figure 6. Anisotropic velocity at the Fermi surface of Cu (see http://www.phy.tu-dresden.de/~fermisur). Minimal velocity 0.72 au (blue areas), maximal velocity 1.26 au (red areas).

determine the conductivity (99)). In particular, the velocity is no longer isotropic as in a free electron model. The amount of the Fermi velocity is strongly anisotropic and varies over a wide range. For Cu as a representative of noble metals the Fermi velocity varies by 50% (figure 6) which is in agreement with experimental data [58, 59]. States with large Fermi velocity (red areas) give a large contribution to the conductivity. The blue areas around the necks are low velocity states. According to equation (90) the amount of the velocity is a measure of the curvature of the band. High velocities result from wide bands whereas low velocities result from narrow bands. The bandwidth, on the other hand, is related to the character of Bloch states.

Using the angular momentum expansion for the Bloch waves (equation (46)) the states can be analysed in terms of angular momenta. Since the Bloch functions are normalized the expansion coefficients fulfil the following condition:

$$\sum_L |\mathring{c}_L(\boldsymbol{k})|^2 = 1. \tag{131}$$

Although, the electronic states are band states which cannot clearly be classified by the quantum number L the square of the expansion coefficients is a measure of the dominating character. In figure 7 the character of states over a Cu Fermi surface is illustrated. The distribution of s, p and d states in Cu is representative for all noble metals. The dominating L character, that is $|\mathring{c}_L(\boldsymbol{k})|^2 \simeq 1$ is visualized by yellow areas at the Fermi surface whereas blue areas correspond to $|\mathring{c}_L(\boldsymbol{k})|^2 \simeq 0$ and indicate a lack of considered angular momentum. Green areas mark $|\mathring{c}_L(\boldsymbol{k})|^2 \simeq 0.5$. The changing colours are related to a continuous transition of $|\mathring{c}_L(\boldsymbol{k})^2|$ between 0 and 1. Obviously, and in contradiction to the common level of understanding states with s character are rare at a noble metal Fermi surface. Remainders are located at the nearly spherical parts of the Fermi surface (figure 7(a)). p states are more pronounced and can be obtained around the van Hove singularities in (100) direction and around the necks (figure 7(b)). All states except states around the van Hove singularities in (100) direction are

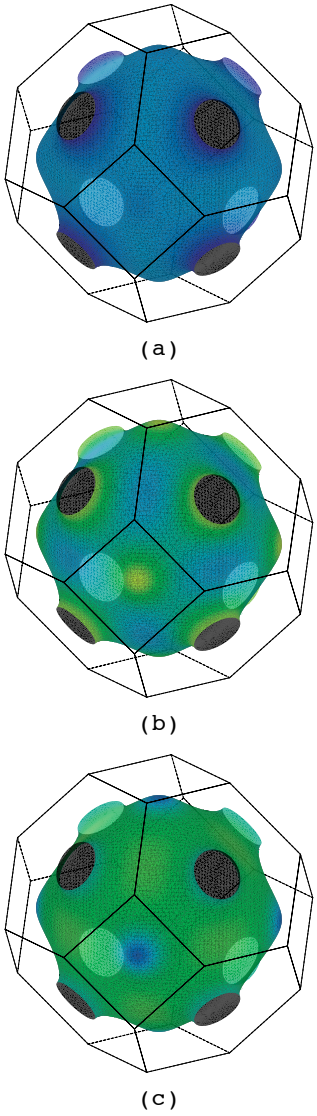

Figure 7. Character of Bloch states at the Fermi surface of Cu (see http://www.phy.tu-dresden.de/~fermisur): (*a*) s character, (*b*) p character and (*c*) d character. The characters change continuously from 0 via 0.5 to 1 which is related to a colour scale of blue via green to yellow.

more than 50% d like (figure 7(*c*)). In the next section we will demonstrate that the character of the wavefunction is extremely important for the understanding of scattering rates.

4.2.2. Impurities in noble metals and residual resistivity. Besides the important influence of the electronic structure of the host material the residual resistivity changes strongly with the type of scatterer. Transition metal impurities, for example, cause a maximum of residual resistivity nearly in the middle of the transition metal series (figure 8) whereas a proportionality to the square of the valance difference ΔZ between host and impurity is obtained for sp impurities, the so-called Linde's rule (figure 9). Another effect related to sp impurities is known as the period effect. The residual resistivity due to impurities with equal ΔZ decreases with increasing atomic number. Empirical models have been introduced to explain the several trends. It will be shown that *ab initio* calculations allow us to understand these trends from a microscopic

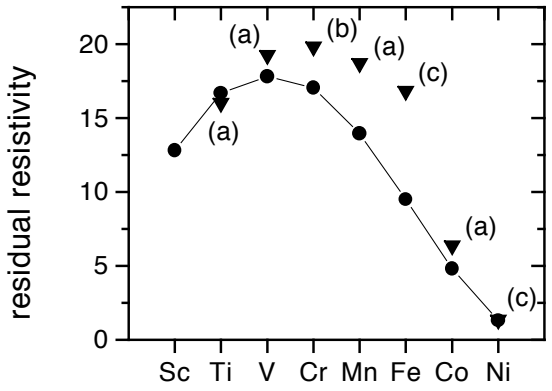

Figure 8. Residual resistivity for 3d transition metal impurities in Cu [8]. Closed circles are theoretical results in comparison with experimental results (triangles) [1].

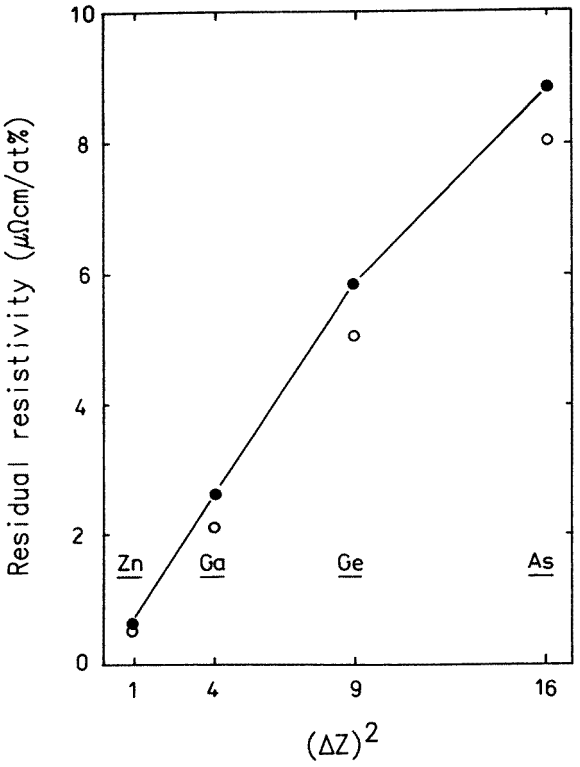

Figure 9. Residual resistivity for sp impurities in Ag [69]. Calculated values (closed circles) in comparison with experimental results (open circles) [1].

level.

By introducing 3d impurities into a noble metal host, the localized 3d level of the impurity atom is, due to the interaction with the conduction electrons, broadened into a resonance, called a virtual bound state after Friedel [60,61]. Friedel's assumptions have been confirmed by self-consistent electronic structure calculations [19] (figure 10). The analysis of local densities of

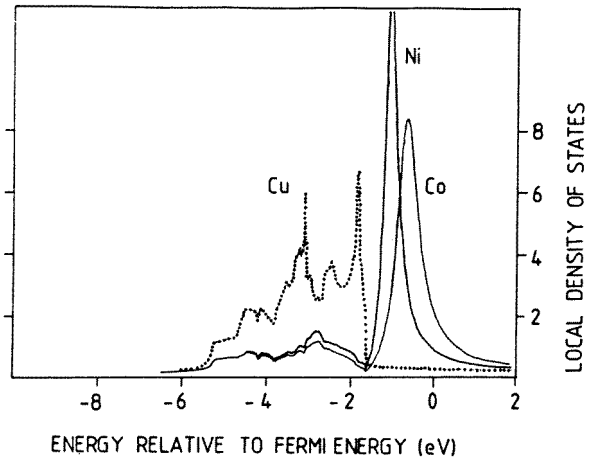

Figure 10. Local densities of states for Ni and Co impurities in Cu together with the host density of states (dotted curve) [19].

states at the impurity site shows clearly that the virtual bound state for an impurity atom at the beginning of the transition metal series is unoccupied and lies far above the Fermi energy [19]. With increasing atomic number, that is, increasing 3d occupation number of the defect the virtual bound state moves from above to below the Fermi energy.

A qualitative explanation of the trend of the resistivity (figure 8) was given by the Friedel–Anderson model [61,62]. The scattering strength is related to the position of the virtual bound state relatively to the Fermi energy. If the virtual bound state is near to the Fermi energy, that appears nearly in the middle of the 3d series, resonance scattering is obtained which leads to large resistivity values. This general trend is reflected in nearly all transport properties as, for example, the residual resistivity of dilute Al [63], Cu [8, 11, 64] and Ag alloys [65], magnetoresistivity and Hall coefficient [66].

Linde's rule can easily be explained. The potential perturbation caused by sp impurities is proportional to the effective charge difference $e\Delta Z$. Consequently, the scattering cross section of the sp impurities is proportional to the square of $e\Delta Z$. This picture was qualitatively discussed by calculations within the free electron model (equation (124)) [67,68] and justified by *ab initio* calculations [69].

The period effect means that for sp defects with equal ΔZ the residual resistivity decreases with increasing atomic number of the defect, that is, the residual resistivity due to defects of the fourth row is larger than that due to defects of the fifth row. This effect is related to the larger impurity radius for higher atomic numbers. The larger impurity radius causes as well as stronger 4d–3d and 5d–3d hybridization, much larger 3d–3d hybridization giving rise to broader impurity states and reduced scattering cross sections.

All these general trends have been confirmed by *ab initio* calculations. Figures 8 [8] and 9 [69] show that theoretical and experimental results are in general agreement. Since the results stem from a calculation using the exact solution of the Boltzmann equation (see section 4.2.1) [8] the differences are connected to the restriction of the impurity charge to a single site.

It should be mentioned, furthermore, that the experimental data for dilute Cu(3d) alloys stem from low temperature experiments ($T = 0$ K). Otherwise, we would not obtain the maximum for Cu(Cr). The considered systems are known to show the Kondo effect which

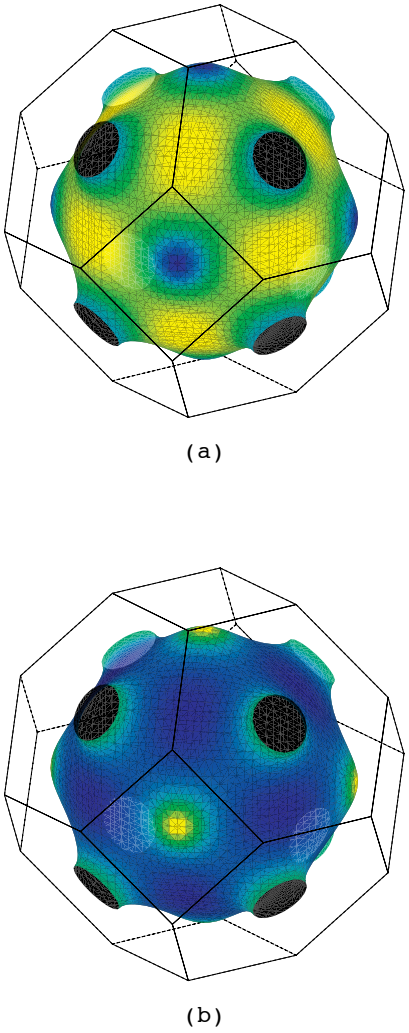

Figure 11. Relaxation time (equation (62)) of (*a*) Cu(Ni) (minimum 0.0002 au, maximum 0.0004 au) and (*b*) Cu(As) (minimum 0.003 au, maximum 0.009 au) dilute alloys. Continuous change from minimal (blue) via medium (green) to maximal (yellow) relaxation times.

is related to a magnetic moment at the impurity site. Consequently, the resistivity is strongly influenced. The resulting effects are related to many body interactions of the electron gas with the impurity atom which are not treated correctly within this theory and will be excluded from this review.

Since *ab initio* calculations do not parametrize the considered properties but describe them at an microscopic level we get detailed information about the underlying processes. For example, the question can be answered which electronic states at the Fermi level contribute to transport? The answer in our last section was that high velocity states are important for conductivity. In this section the interaction with the impurity is discussed.

The easiest way to characterize scattering is by means of the relaxation time. Large relaxation time means weak scattering (yellow areas in figure 11) and large contribution to conductivity, low resistivity. Electrons within states of small relaxation time undergo a strong scattering (blue areas in figure 10) and will give a small contribution to conduction. The distribution of relaxation times over the Fermi surface is shown for a Ni impurity as a representative of a d scatterer (figure 11(*a*)) and for a As impurity, a typical sp scatterer

Table 1. Comparison of exact solution (I—equation (97)) and relaxation time approximations (II—equation (121) and III—equation (122)) of the Boltzmann equation.

	ρ in $\mu\Omega$ cm/at%		
System	I	II	III
Cu(Ni)	1.41	1.61	1.61
Cu(As)	4.96	7.60	7.41

(figure 11(*b*)). The figures demonstrate first of all that the anisotropy of the scattering rate depends strongly on the type of scattering potential and can vary by an order of magnitude over the Fermi surface. Furthermore, the type of impurity potential determines which states are influenced by scattering. A Ni defect with impurity d states causes strong scattering of Bloch electrons with d character (see blue areas in figure 11(*a*) in comparison to figure 7(*c*)) which is already known from the investigation of magnetic-field-induced surface states [70–72]. The opposite behaviour is obtained for Cu(As) (see figure 11(*b*)). The impurity levels are sp like consequently the Bloch electrons with sp character undergo strong scattering (figures 7(*a*) and (*b*)).

To summarize, conduction is an interplay of pure bandstructure and scattering. Electrons with large velocity are of course designated for carrying the current. But this is strongly influenced by the scattering properties of the impurity potential. This tendency can be amplified or reversed by the relaxation time and the scattering-in term (equation (97)).

The scattering-in term contributes to the amount of the vector mean free path. Generally, Λ increases up to 10% in comparison to τv for transition metal impurities and up to 50% for sp impurities. This discussion is also reflected in table 1 where a comparison of the full solution (equation (97)) and the relaxation time approximations (equations (121), (122)) is presented. The relaxation time approximation works well for transition metal defects in Cu whereas for sp defects in Cu the results of the relaxation time approximation can be wrong by a factor of two. This is, of course, related to the relaxation times (figure 11). Transition metal impurities in noble metals cause a more isotropic scattering than sp impurities since the d states are more equally distributed over the Fermi surface than the sp states.

4.3. Ferromagnetic systems

The transport properties of ferromagnetic dilute alloys have been intensively investigated about 20 years ago. These experimental results revive since the discovery of giant magnetoresistance in magnetic multilayers [73,74]. They provide a good basis to understand the new phenomenon.

Theoretical explanations of the experiments have been given using Mott's two current model. Following Mott's idea [50] several transport properties of ferromagnetic alloys (see figure 3) can be explained by assuming conduction in parallel by electrons in the majority bands (spin-up electrons) and by electrons in the minority bands (spin-down electrons). The physical basis of this two current model is the dominance of spin-conserving potential scattering and the weakness of spin-flip collisions in a ferromagnetic alloy at low temperatures (see discussion in section 2.2.6). It seems that the model provides a good basis for the discussion of a wide range of alloy properties [75]. Owing to the developments of density-functional theory and sophisticated numerical techniques we are now able to perform realistic *ab initio* calculations which puts us in position to check the reliability of the above-mentioned model studies and to elucidate the undergoing microscopic processes. Theoretical studies of ferromagnetic dilute alloys performed within the Green function method [56,76–80] presented a detailed analysis of

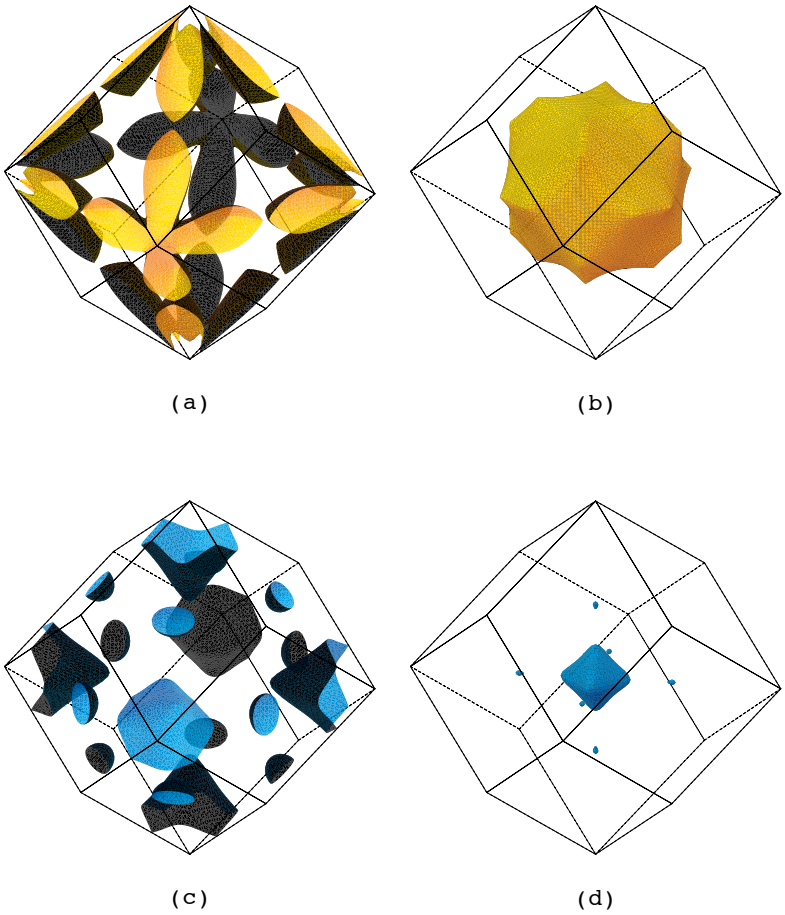

Figure 12. Fermi surface of bcc Fe (see http://www.phy.tu-dresden.de/~fermisur). Majority sheet: (*a*) $h_5^{\uparrow}$, (*b*) $e_6^{\uparrow}$. Minority sheet: (*c*) $e_3^{\downarrow}$, (*d*) $e_4^{\downarrow}$.

the range of charge and magnetization perturbations around the impurities. The extension of the formalism to transport properties of dilute Fe, Co and Ni alloys was given in [12, 21, 81–83]. To review the data and demonstrate the peculiarities of transport in ferromagnetic systems results of dilute Fe, Co and Ni alloys are summarized in this chapter.

4.3.1. Fermi surfaces. In magnetic systems the spin degeneracy of the energy eigenvalues is lifted, states are exchange split. Consequently, the systems have a magnetic moment (equation (29)) which is $2.2\mu_B$/atom for Fe, $1.6\mu_B$/atom for Co and $0.6\mu_B$/atom for Ni. The majority band of the ferromagnets is occupied except for bcc Fe. For Fe the Fermi energy cuts off the upper shoulder from the d states so that about 0.2–0.3 d states are not occupied (see figure 15). For fcc Co (figure 16) and Ni (figure 17) the Fermi energy lies above the majority d band. The minority-spin density of states is characterized by the fact that the Fermi energy falls into the minority d band. From Fe to Ni the number of occupied minority d states increases thus the magnetic moment decreases.

This behaviour is also reflected in the Fermi surfaces. Indeed, the Fermi surfaces of Fe (figure 12), Co (figure 13) and Ni (figure 14) are multisheeted and reflect the lattice structure.

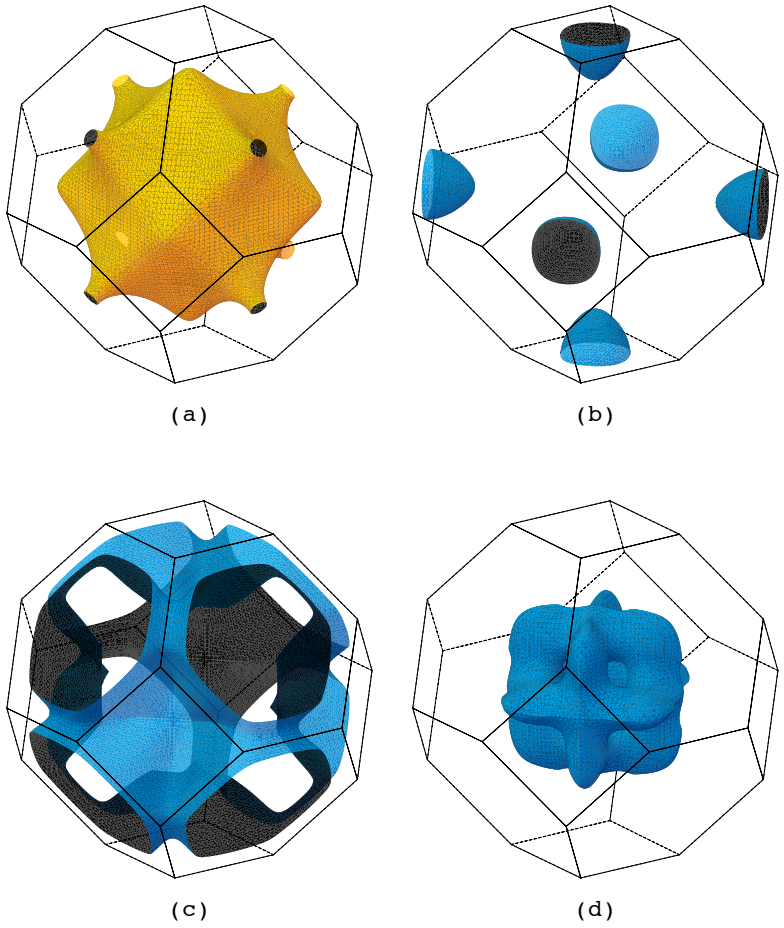

Figure 13. Fermi surface of fcc Co (see http://www.phy.tu-dresden.de/∼fermisur). Majority sheet: (*a*) $e_6^{\uparrow}$. Minority sheets: (*b*) $h_3^{\downarrow}$, (*c*) $e_4^{\downarrow}$, (*d*) $e_5^{\downarrow}$.

We distinguish the Fermi surfaces of the majority electrons (yellow) and minority ones (blue). Since the majority d band in Co (figure 13) and Ni (figure 14) is occupied the Fermi surface consists of one sheet that is very similar to the Cu Fermi surface and less inflated since one electron is missed. In Fe, however, two majority sheets are obtained (figure 12) since the d band is not fully occupied. The minority Fermi surface consists of many electron and hole sheets due to the partially filled d band (shown in figures 12–14). The third, fourth and fifth minority band of Co and Ni are directly related to each other and reflect the increasing occupation of d states going from Co to Ni. Generally, the nearly occupied bands that give rise to hole pockets (figures 13(*b*), 14(*b*) and (*c*)) around the (100) points of the Brillouin zone are less important for conduction. In contrast, the large electron-like ones contribute considerably to conductivity.

The illustration of the calculated Fermi velocity distribution and the character of the electronic states would be too expensive and space consuming within this review. But they are presented the same way as discussed for Cu (section 4.2)†. Summing up these properties, it

† see web page http://www.phy.tu-dresden.de/∼fermisur.

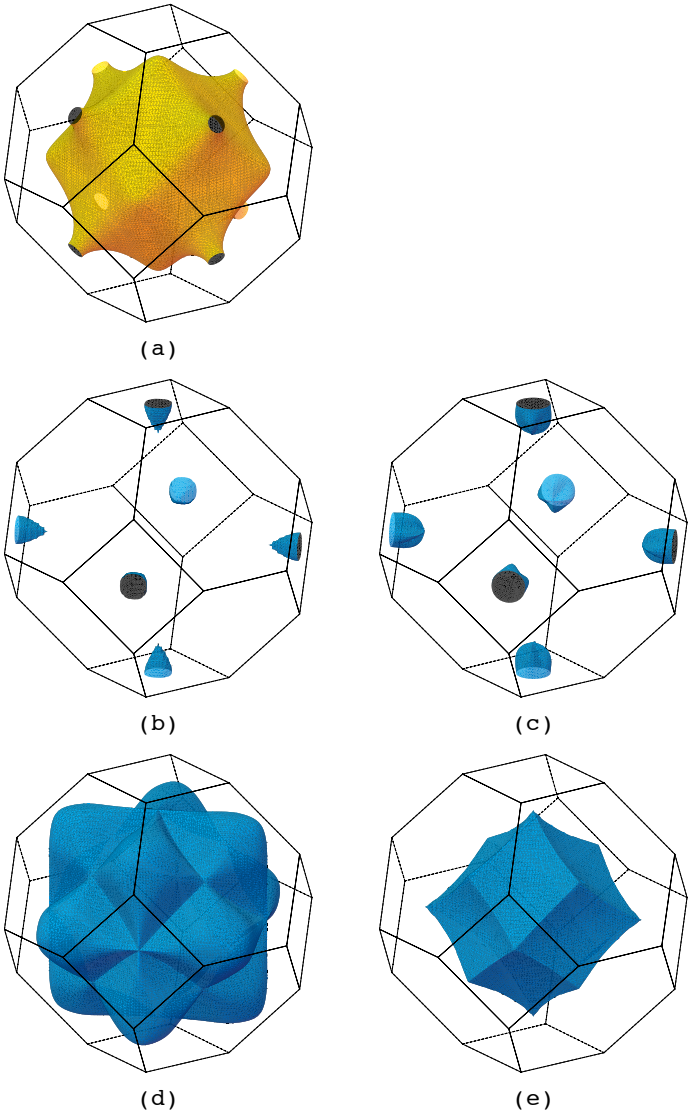

Figure 14. Fermi surface of fcc Ni (see http://www.phy.tu-dresden.de/∼fermisur). Majority sheet: (*a*) $e_6^{\uparrow}$. Minority sheets: (*b*) $h_3^{\downarrow}$, (*c*) $h_4^{\downarrow}$, (*d*) $e_5^{\downarrow}$, (*e*) $e_6^{\downarrow}$.

may be said that the distributions of Fermi velocity and character of states are as complicated as the topology of the Fermi surface itself, i.e. they reflect details of the electronic structure in the same way as was discussed for Cu and that both distributions are far from being isotropic.

4.3.2. Impurities in ferromagnetic systems. A key to understanding the scattering properties of an impurity atom is the local density of states, that is, the change of the electronic structure at the defect site (see also equation (37)). Compared with the results of a noble metal host (see section 4.2.2) the situation is a little more complicated since the defect acts differently in both spin bands. The resulting local densities of states in the impurity Wigner–Seitz spheres

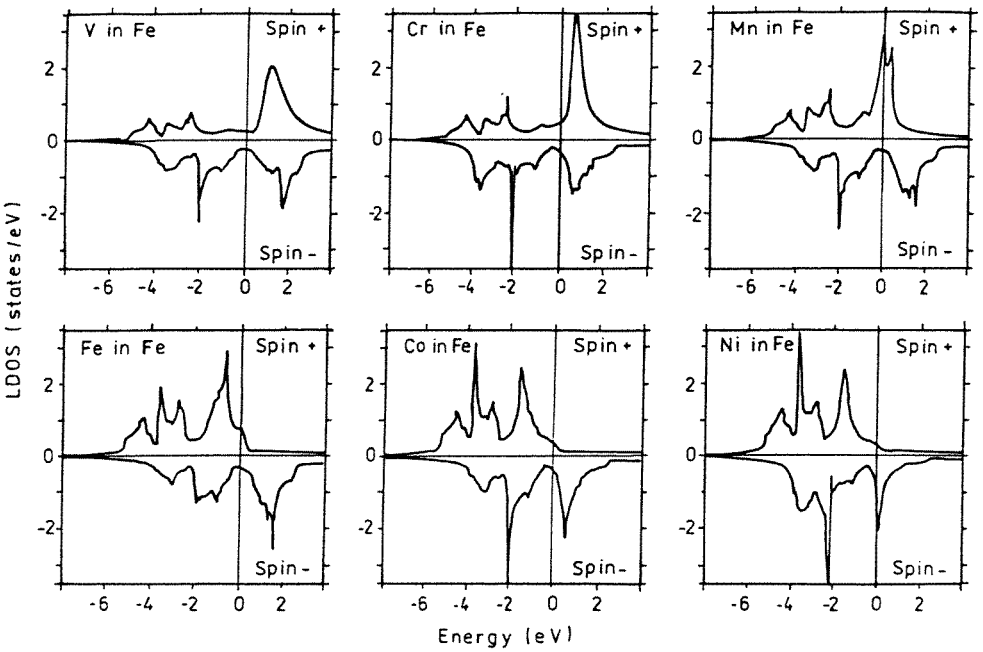

Figure 15. Local densities of states of 3d impurities in Fe for both spin directions (see [42]). The figure denoted Fe in Fe represents the density of states of pure Fe.

for ferromagnetic dilute alloys are shown in figure 15 for Fe(3d), in figure 16 for Co(3d) and figure 17 for Ni(3d), respectively. It should be mentioned that the calculations have been performed including the charge relaxation at the next nearest neighbour sites. The important changes concerning transport, however, occur at the impurity site. The results for both spin directions are plotted with the energies given relative to the Fermi energy. The host density of states is also given as a reference system (denoted as Fe in Fe, Co in Co and Ni in Ni). These results are chosen from a variety of systems [56, 76–80] to discuss the general trends of microscopic processes and to review the data with respect to the magnetic multilayers showing interlayer exchange coupling [84] and giant magnetoresistance [85, 86]. The actual electronic structure of the perturbed system is determined by the valence difference and by the difference in the magnetic moments between host and impurity atom. As a consequence spectral weight is moved and impurity virtual bound states are formed either in the majority or/and minority band at a characteristic energy. Analysing these results the following general trends are obtained.

- Impurities with $\Delta Z \leqslant |2|$ produce nearly no change in the majority band. The charge adjustment is achieved by the minority band alone.
- Impurities with $\Delta Z < -2$ produce a virtual bound state in the majority band at E_F or an empty virtual bound state above E_F. The population of the minority states does not change very much any more.
- For impurities with $\Delta Z > 2$ we obtain the tendency that both spin bands are more and more filled up to accommodate the additional charge.

As a consequence of the changed electronic structure the magnetic moments at the defect sites are varied (equation (40)). Using the above discussed formalism the impurity moments can be calculated with high accuracy. A comparison of theoretical and experimental impurity moments is given in [42] for Fe(3d), in [80] for Co(3d) and in [77] for Ni(3d).

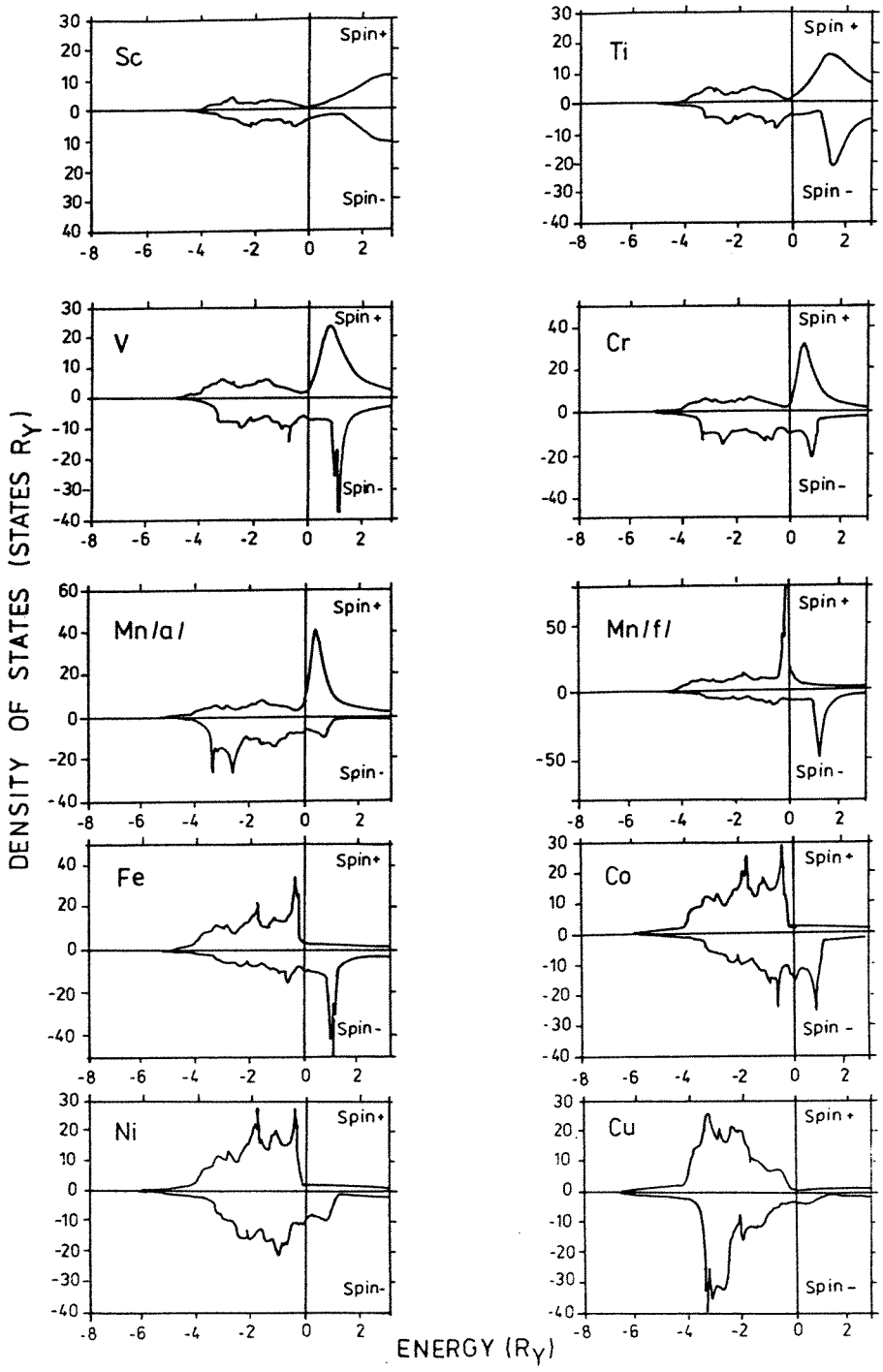

Figure 16. Local densities of states of 3d impurities in Co for both spin directions (see [80]). The figure denoted Co in Co represents the density of states of pure Co. Mn is shown for both magnetic configurations.

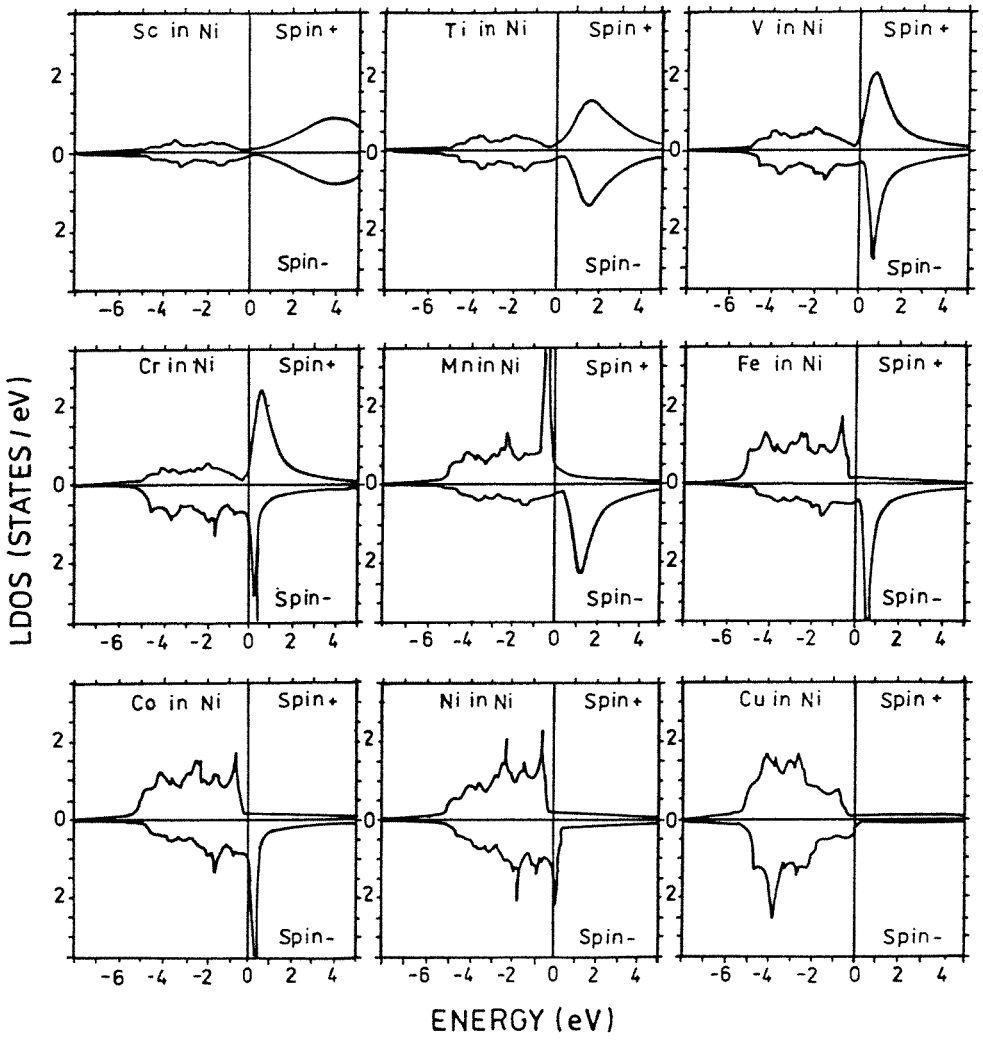

Figure 17. Local densities of states of 3d impurities in Ni for both spin directions (see [56]). The figure denoted Fe in Fe represents the density of states of pure Fe.

Concerning the scattering cross sections of impurity atoms in ferromagnetic hosts the changes of the local density of states at the Fermi energy are important. In general, the resonance concept discussed for noble metal hosts yields for each spin-band separately. Strong scattering in one spin channel is obtained if the impurity virtual bound state lies at the Fermi level or if spectral weight is moved to or removed from the Fermi energy with respect to the unperturbed system.

4.3.3. Residual resistivity and spin anisotropy ratios. The results for the residual resistivities of 3d impurities in the ferromagnets Fe, Co and Ni are shown in figures 18(*a*)–20(*a*), respectively, in comparison to experimental results. Taking into consideration, first, that the calculations are done without any free parameter and second, that the obtained experimental results scatter over a wide range, the agreement is surprisingly good and demonstrates the

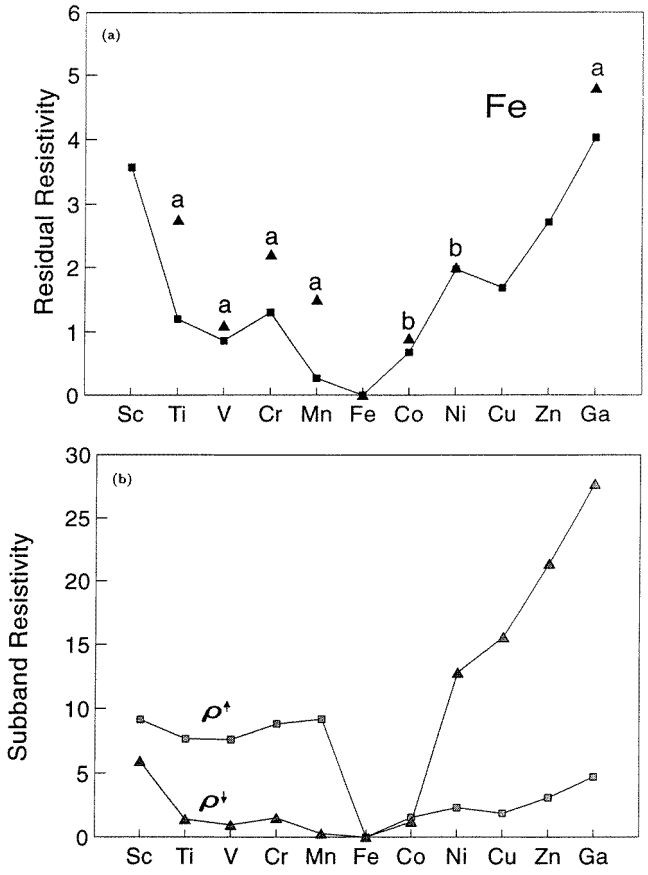

Figure 18. (*a*) Calculated residual resistivities for 3d impurities in Fe in comparison to experimental data in $\mu\Omega$ cm/at%, a: [88], b: [89, 90]. (*b*) Sub-band resistivities $\rho^{\uparrow}$ (full line) and $\rho^{\downarrow}$ (broken line) in $\mu\Omega$ cm/at%.

reliability of the *ab initio* calculations.

The trends of the residual resistivities for the different ferromagnetic hosts with 3d transition metal impurities can be understood by means of a sub-band decomposition according to Mott's two current model which is shown in figures 18(*b*)–20(*b*). The trends of the spin channels, $\rho^{\uparrow}$ and $\rho^{\downarrow}$, reflect the scattering properties which have been discussed in the last section. For example, resonance scattering is the origin of the high resistivity values in the majority band for Fe(Mn), Co(Mn) and Ni(Cr). Since the majority Fermi surface of Co and Ni is noble metal-like $\rho^{\uparrow}$ increases according to Linde's rule for systems with $\Delta Z \leqslant |2|$.

The total resistivity is, of course, determined by the low resistivity channel. This proportion changes sensitively as a function of valance difference between host and impurity atom and is described by the spin-anisotropy ratio α given in equation (103). Experimentally, this information cannot be obtained from the resistivities since the components of the resistivity tensor are scalars. The anisotropy values can only be deduced if the measurements are done with respect to a reference system, for example, in ternary alloys [75]. The meaning of the anisotropy ratios is illustrated schematically in figure 21. $\alpha \ll 1$ means that the minority electrons determine the total resistivity since they are only weakly scattered by the defect and form a fast, highly conducting channel. $\alpha \gg 1$ is opposite. Now the majority electrons are

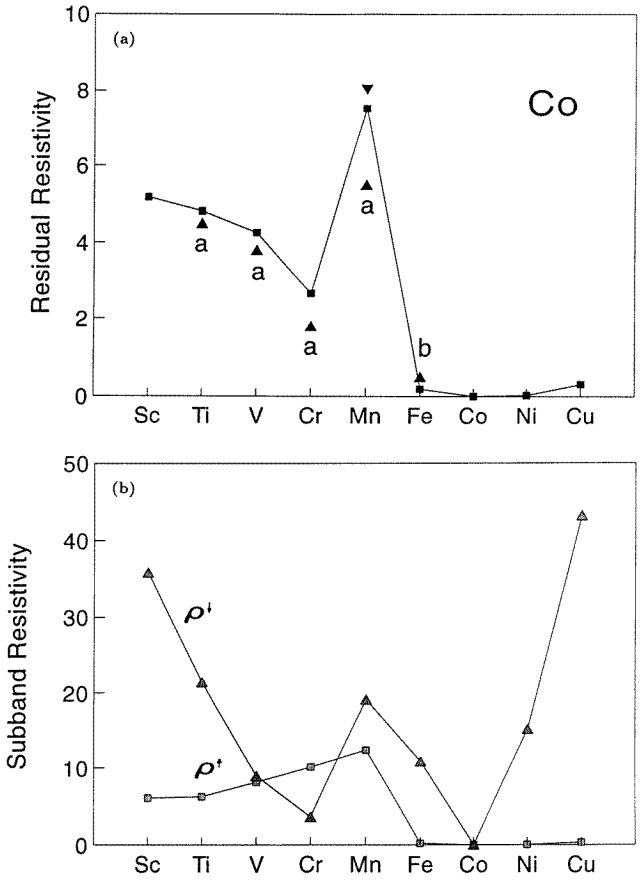

Figure 19. (*a*) Calculated residual resistivities for 3d impurities in Co in comparison to experimental data in $\mu\Omega$ cm/at%, a: [91], b: [92]. (*b*) Sub-band resistivities $\rho^{\uparrow}$ and $\rho^{\downarrow}$ in $\mu\Omega$ cm/at%.

faster and determine the total resistivity. The calculated and measured anisotropy ratios are given in tables 2–4. The agreement is again very good and the calculated values are reliable and can be used as prediction except for systems with the valance difference between host and impurity atom $\Delta Z \leqslant |2|$. These are the so-called short circuit systems. The electronic structure of the majority band is not influenced by these defects, though, the calculated resistivity is going to be zero for this band and produces a short circuit. This behaviour is, of course, an artifact of the non-relativistic calculation. Spin–orbit coupling and, consequently, spin-flip scattering are neglected although they are important in these systems. Although, the spin-flip scattering contribution is small it would change the resistivity of the majority band from zero to a finite value and the short circuit effect disappears. A fully relativistic *ab initio* treatment overcomes this problem [87].

The anisotropy ratios have been introduced to explain the residual resistivities of ferromagnetic dilute alloys [75].

Furthermore, in some cases $1/\alpha_{\text{theor}}$ is in better agreement than α_{theor}. It might be within the experimental error since all values are near to 1.

Finally it should be mentioned again that the anisotropy ratios are still very useful nowadays to understand the resistivities and giant magnetoresistance in magnetic multilayers [73],

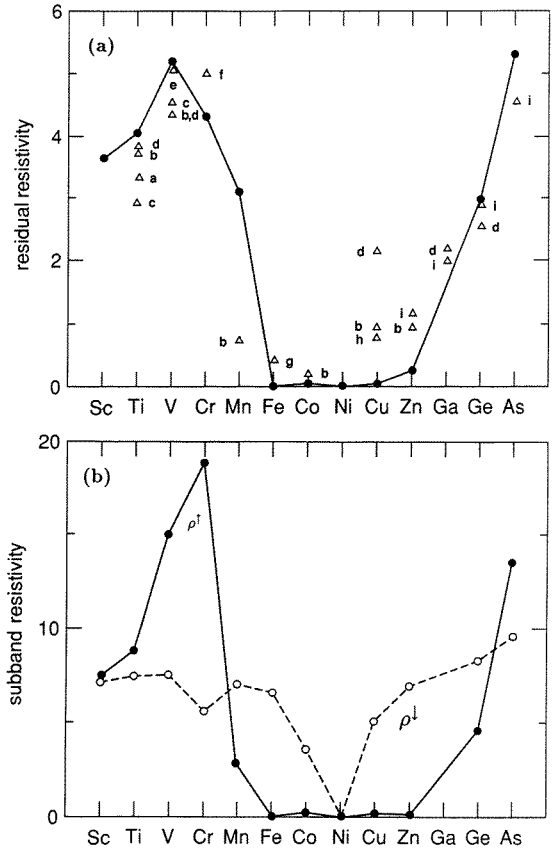

Figure 20. (*a*) Calculated residual resistivities for 3d and 4sp impurities in Ni in comparison to experimental data in $\mu\Omega$ cm/at%, a: [89], b: [88], c: [93], d: [93], e: [94], f: [95], g: [96], h: [97], i: [98], j: [92], k: [99], l: [100] m: [101]. (*b*) Sub-band resistivities $\rho^{\uparrow}$ (full curve) and $\rho^{\downarrow}$ (broken curve) in $\mu\Omega$ cm/at%.

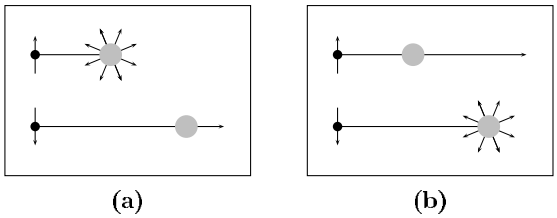

Figure 21. Spin anisotropy of impurity scattering: (*a*) $\alpha \ll 1$ and (*b*) $\alpha \gg 1$.

especially the so-called inverse giant magnetoresistance [85, 86]. The spin-anisotropy ratios act as data base to tailor new multilayers with defined properties.

5. Conclusion

An *ab initio* method to calculate the transport properties of dilute alloys was presented and reviewed. The method is based on density functional theory using a Green function formulation

Table 2. Anisotropy ratios $\alpha = \rho^{\downarrow}/\rho^{\uparrow}$ of dilute Fe alloys.

Impurity	α_{theor}	$(1/\alpha_{\text{theor}})$	α_{exp}
Sc	0.65	—	—
Ti	0.19	—	0.25[a], 0.66[b]
V	0.13	—	0.12[a], 0.13[b]
Cr	0.17	—	0.17[a], 0.37[b]
Mn	0.03	—	0.09[a], 0.17[b]
Co	0.77	1.30	1.0[a], 3.7[b]
Ni	5.48	—	3.0[a], 7.0[b]
Y	1.50	—	—
Zr	0.88	—	—
Nb	0.61	—	—
Mo	0.61	—	0.21[b]
Tc	0.51	—	—
Ru	0.58	—	0.38[b]
Rh	5.59	—	5.8[b]
Pd	11.61	—	—
Cu	8.20	—	—
Zn	6.87	—	—
Ga	5.87	—	—
Ag	12.22	—	—
Cd	7.69	—	—

[a] [88].
[b] [89,90].

Table 3. Anisotropy ratios $\alpha = \rho^{\downarrow}/\rho^{\uparrow}$ of dilute Fe alloys.

Impurity	α_{theor}	$(1/\alpha_{\text{theor}})$	α_{exp}
Sc	5.94	—	—
Ti	3.44	—	1.4[b]
V	1.1	—	1.0[b]
Cr	0.35	—	0.3[b]
Mn_{af}	1.49	0.67	0.8[b]
Mn_{f}	1.54	0.64	0.8[b]
Fe	57.66	—	12[a]
Ni	522.41	—	—
Cu	139.35	—	—
Y	3.22	—	—
Zr	2.50	—	3.3[b]
Nb	1.51	—	1.0[b]
Mo	0.68	—	0.7[b]
Tc	0.20	—	—
Ru	0.05	—	0.22[a]
Rh	0.94	1.06	1.0[b]
Pd	299.07	—	—
Ag	205.55	—	—

[a] [91].
[b] [92].

to determine the electronic structure of the dilute alloy. To obtain the transport properties without any free parameter the Boltzmann equation was solved taking the anisotropic electronic structure and the anisotropic impurity scattering matrix elements into consideration.

Table 4. Anisotropy ratios $\alpha = \rho^{\downarrow}/\rho^{\uparrow}$ of dilute Ni alloys.

Impurity	α_{theor}	$(1/\alpha_{\text{theor}})$	α_{exp}
Sc	0.97	—	—
Ti	0.85	1.17	1.1[a], 4[b], 2.7[d]
V	0.53	—	0.45[a], 0.55[b], 2.3[d]
Cr	0.30	—	0.5[a], 0.45[b], 0.4[c], 0.21[d], 0.2[f], 0.4[g]
Mn	2.42	—	8.9[a], 15[b], 5.4[d]
Fe	—	—	11[a], 20[b], 7.3[d]
Co	92.4	—	13[a], 30.5[b], 20[c], 13[d], 20[f], 20[g]
Y	0.60	—	—
Zr	0.64	1.56	7.5[e]
Nb	0.54	—	0.44[e], 0.47[i]
Mo	0.31	—	0.28[e], 0.37[i]
Tc	0.11	—	—
Ru	0.17	—	0.29[a], 0.15[e]
Rh	0.77	—	0.65[a], 0.17[e], 0.29[i]
Pd	0.19	—	1[d]
Cu	250.0	—	2.9[a], 3.7[d]
Zn	24.0	—	2.2[a]
Ga	—	—	1.7[g]
Ge	1.82	—	1[g]
As	0.71	—	—
Ag	24.0	—	—
Cd	15.2	—	—
In	0.51	1.96	1.5[h]
Sn	0.24	—	1.6[a], 1.35[h]
Sb	—	—	0.8[h]

[a] [89],
[b] [88].
[c] [102].
[d] [103].
[e] [104].
[f] [99].
[g] [98].
[h] [100].
[i] [92].

The high quality of the method was demonstrated by reviewing a wide range of data. The results confirm phenomenological models, extend the potential to explain details and trends of the experimental data and increase our knowledge about microscopic processes behind the macroscopic transport properties. The accuracy of the method opens the opportunity for a future theoretical material design.

Acknowledgments

I thank P H Dederichs, R Zeller, P Zahn and J Binder for stimulating discussions and for their collaboration. In addition, I wish to acknowledge and thank A Fert, P Levy and K Becker. Finally, I acknowledge with gratitude grants from the DFG, Me1153/6-1 and SFB422, from BMBF Contract no 65621 ODA 7 and NATO Grant no CRG9603440.

References

[1] Landolt-Börnstein 1982 *Metals: Electronic Transport Phenomena* vol 15 (Berlin: Springer)
[2] Doniach S and Sondheimer E H 1974 *Green's Functions for Solid State Physicists* (London: Benjamin)
[3] Mahan G D 1981 *Many-Particle Systems* (New York: Plenum)
[4] Kubo R, Toda M and Hashitsume N 1985 *Statistical Physics II: Nonequilibrium Statistical Mechanics* (Berlin: Springer)
[5] Kubo R 1957 *J. Phys. Soc. Japan* **12** 570
[6] Greenwood D A 1958 *Proc. Phys. Soc.* **71** 585
[7] Mahan G D 1987 *Phys. Rep.* **145** 251
[8] Mertig I, Mrosan E and Schöpke R 1982 *J. Phys. F: Met. Phys.* **12** 1689
[9] Butler W H 1985 *Phys. Rev.* B **31** 3260
[10] Swihart J C *et al* 1986 *Phys. Rev. Lett.* **57** 1181
[11] Ek J V and Lodder A 1990 *Solid State Commun.* **73** 373
[12] Mertig I, Zeller R and Dederichs P H 1993 *Phys. Rev.* B **47** 16178
[13] Banhart J, Ebert H, Voitländer J and Weinberger P 1994 *Phys. Rev.* B **50** 2104
[14] Dupree T H 1961 *Ann. Phys., NY* **15** 63
[15] Beeby J L 1967 *Proc. R. Soc.* A **302** 113
[16] Holzwarth N A W 1975 *Phys. Rev.* B **11** 3718
[17] Lehmann G 1983 *Ergebnisse in der Elektronentheorie der Metalle* ed P Ziesche and G Lehmann (Berlin: Akademie) p 127
[18] Zeller R, Podloucky R and Dederichs P H 1980 *Z. Phys.* B **38** 165
[19] Dederichs P H and Zeller R 1981 Festkörperprobleme *Adv. Solid State Phys.* **XXI** 243
[20] Mertig I, Mrosan E and Ziesche P 1987 *Multiple Scattering Theory of Point Defects in Metals: Electronic Properties* (Leipzig: Teubner)
[21] Mertig I 1994 *Habitilationsschrift* TU Dresden
[22] Born M and Oppenheimer J R 1927 *Ann. Phys.* **84** 457
[23] Hohenberg P and Kohn W 1964 *Phys. Rev.* **136** 864
[24] Kohn W and Sham L J 1965 *Phys. Rev.* **140** 1133
[25] Sham L J and Kohn W 1966 *Phys. Rev.* **145** 561
[26] Janak J F 1978 *Phys. Rev.* B **12** 7165
[27] Rajagopal A K 1980 *Adv. Chem. Phys.* **41** 59
[28] Hedin L and Lundqvist B 1971 *J. Phys. C: Solid State Phys.* **4** 2064
[29] Barth U V and Hedin L 1972 *J. Phys. C: Solid State Phys.* **5** 1629
[30] Moruzzi V R, Janak J F and Williams A R 1978 *Calculated Electronic Properties of Metals* (New York: Pergamon)
[31] Gunnarsson O, Lundqvist B I and Lundqvist S 1972 *Solid State Commun.* **11** 149
[32] Gunnarsson O and Lundqvist B I 1976 *Phys. Rev.* B **13** 4274
[33] Vosko S H, Wilk L and Nussair N 1980 *Can. J. Phys.* **58** 1200
[34] Terakura K 1976 *J. Phys. Soc. Japan* **40** 450
[35] Terakura K 1976 *J. Phys. F: Met. Phys.* **6** 1385
[36] Terakura K 1977 *Physica* B **91** 162
[37] Oppeneer P M and Lodder A 1987 *J. Phys. F: Met. Phys.* **17** 1885
[38] Oppeneer P M and Lodder A 1987 *J. Phys. F: Met. Phys.* **17** 1901
[39] Mattheiss L F 1964 *Phys. Rev.* **133** A1399
[40] Mattheiss L F 1964 *Phys. Rev.* **134** A970
[41] Zeller R 1987 *J. Phys. C: Solid State Phys.* **20** 2347
[42] Drittler B, Weinert M, Zeller R and Dederichs P H 1989 *Phys. Rev.* B **39** 930
[43] Lloyd P 1967 *Proc. Phys. Soc.* **90** 207
[44] Braspenning P J, Zeller R, Lodder A and Dederichs P H 1984 *Phys. Rev.* B **29** 703
[45] Fert A 1969 *J. Phys. C: Solid State Phys.* **2** 1784
[46] Bourquart A, Daniel E and Fert A 1968 *Phys. Lett.* A **26** 260
[47] Monod P 1968 *PhD Thesis* Universite Paris-Sud, Paris
[48] Ziman J M 1962 *Electrons and Phonons* (London: Oxford University Press)
[49] Velicky B 1969 *Phys. Rev.* B **184** 614
[50] Mott N F 1964 *Adv. Phys.* **13** 325
[51] Sondheimer D 1962 *Proc. R. Soc.* A **268** 100
[52] Coleridge P T 1972 *J. Phys. F: Met. Phys.* **2** 1016

[53] Korringa J 1947 *Physica* **13** 392
[54] Kohn W and Rostoker N 1954 *Phys. Rev.* **94** 1111
[55] Lehmann G and Taut M 1972 *Phys. Status Solidi* B **54** 469
[56] Zeller R 1987 *J. Phys. F: Met. Phys.* **17** 2123
[57] Zahn P 1994 *Diplomarbeit* TU Dresden
[58] Doezema R E and Koch J F 1972 *Phys. Rev.* B **5** 3866
[59] Mitchell J W and Goodrich R G 1985 *Phys. Rev.* B **32** 4969
[60] Friedel J 1958 *J. Phys. Radium* **19** 573
[61] Friedel J 1958 *Suppl. Nuovo Cimento* **VII** 287
[62] Anderson P W 1961 *Phys. Rev.* **124** 41
[63] Schöpke R and Mrosan E 1978 *Phys. Status Solidi* b **90** K95
[64] Lodder A et al 1986 *Phys. Status Solidi* b **135** 831
[65] Mertig I, Mrosan E, Zeller R and Dederichs P H 1983 *Phys. Status Solidi* b **117** 619
[66] Mertig I and Mrosan E 1983 *J. Phys. F: Met. Phys.* **13** 373
[67] Blatt F J 1957 *Phys. Rev.* **108** 286
[68] Blatt F J 1957 *Phys. Rev.* **108** 1204
[69] Vojta T, Mertig I and Zeller R 1992 *Phys. Rev.* B **46** 15751
[70] Baratta A J and Ehrlich A C 1981 *Phys. Rev.* B **24** 517
[71] Baratta A J and Ehrlich A C 1983 *Phys. Rev.* B **28** 4136
[72] Graefenstein J, Mertig I, Mrosan E and Zeller R 1988 *J. Phys. F: Met. Phys.* **18** 731
[73] Baibich M N *et al* 1988 *Phys. Rev. Lett.* **61** 2472
[74] Binash G, Grünberg P, Saurenbach F and Zinn W 1989 *Phys. Rev.* B **39** 4828
[75] Campbell I A and Fert A 1982 *Ferromagnetic Materials* (New York: North-Holland,) ch 9, p 747
[76] Blügel S, Akai H, Zeller R and Dederichs P H 1987 *Phys. Rev.* B **35** 3271
[77] Stefanou N, Oswald A, Zeller R and Dederichs P H 1987 *Phys. Rev.* B **35** 6911
[78] Drittler B *et al* 1989 *Phys. Rev.* B **40** 8203
[79] Akai I, Akai M and Kanamori J 1985 *J. Phys. Soc. Japan* **54** 4257
[80] Stepanyuk V S, Zeller R, Dederichs P H and Mertig I 1994 *Phys. Rev.* B **49** 5157
[81] Mertig I, Zeller R and Dederichs P H 1994 *Metallic Alloys: Experimental and Theoretical Perspectives* ed J S Faulkner and R Jordan (Dordrecht: Kluwer) p 423
[82] Mertig I et al 1995 *J. Magn. Magn. Mater.* **151** 363
[83] Mertig I 1996 *NATO ASI Series* B **355** 265
[84] Parkin S S P 1991 *Phys. Rev. Lett.* **67** 3598
[85] George J M et al 1994 *Phys. Rev. Lett.* **72** 408
[86] Hsu S Y et al 1997 *Phys. Rev. Lett.* **78** 2652
[87] Banhart J, Vernes A and Ebert H 1996 *Solid State Commun.* **98** 129
[88] Fert A and Campbell I A 1976 *J. Phys. F: Met. Phys.* **6** 849
[89] Dorleijn J F and Miedema A R 1975 *J. Phys. F: Met. Phys.* **5** 487
[90] Dorleijn J F 1976 *Philips Res. Rep.* **31** 287
[91] Loegel B and Gautier F 1971 *J. Phys. Chem. Sol.* **32** 2723
[92] Durand J 1973 *PhD Thesis* Université Louis Pasteur, Strasbourg
[93] Beylin V M, Zeynalov T I, Rogelberg I L and Cherenkov V A 1978 *Fiz. Met. Metalloved.* **46** 1083
[94] Arajs A, Chessin H and Colvin R V 1964 *Phys. Status Solidi* b **7** 1009
[95] Schwerer F C and Conroy J W 1971 *J. Phys. F: Met. Phys.* **1** 877
[96] Farrell T and Greig D 1968 *J. Phys. C: Solid State Phys.* **1** 1359
[97] Greig D and Rowlands J A 1974 *J. Phys. F: Met. Phys.* **4** 232
[98] Hugel J 1973 *J. Phys. F: Met. Phys.* **3** 1723
[99] Cadeville M C, Gautier F, Robert C and Roussel J 1968 *Solid State Commun.* **7** 1701
[100] Ross R N, Price D C and Williams G 1979 *J. Magn. Magn. Mater.* **10** 59
[101] Price D C and Williams G 1973 *J. Phys. F: Met. Phys.* **3** 810
[102] Leonard P, Cadeville M C, Durand J and Gautier F 1969 *J. Phys. Chem. Solids* **30** 2169
[103] Farrell T and Greig D 1969 *J. Phys. C: Solid State Phys.* **2** 1465
[104] Durand J and Gautier F 1970 *J. Phys. Chem. Solids* **31** 2773